ACS EARTH AND SPACE CHEMISTRY

http://pubs.acs.org/journal/aesccq

Article

Crystal Chemistry and Thermodynamics of HREE (Er, Yb) Mixing in a Xenotime Solid Solution

Andrew C. Strzelecki, Margaret Reece, Xiaodong Zhao, Wendy Yu, Chris Benmore, Yang Ren, Christopher Alcorn, Artaches Migdisov, Hongwu Xu, and Xiaofeng Guo*

Cite This: *ACS Earth Space Chem.* 2022, 6, 1375−1389

Read Online

ACCESS | Metrics & More | Article Recommendations | Supporting Information

ABSTRACT: Rare earth elements (REEs), the 15 naturally occurring lanthanides plus yttrium and scandium, are ubiquitously used in modern life as they are critical components of many advanced devices and technologies. However, the demand for REEs is not equal, with the heavy rare earth elements (HREEs) having a higher demand. Xenotime ($HREEPO_4$) is an important HREE ore mineral and globally is an economical source of HREE. Most of the crystallographic and thermodynamic properties of xenotime endmembers have been elucidated by calorimetric, solubility, and high-pressure studies. Yet, in natural systems, endmembers are rarely encountered, and instead, REE solid solutions are more commonly observed. In this work, we characterize the crystal chemistry, thermodynamics of HREE mixing, and high-temperature material behaviors and thermochemistry of a synthetic erbium (Er)−ytterbium (Yb) binary xenotime solid solution ($Er_{(x)}Yb_{(1-x)}PO_4$) using a suite of experimental techniques, including X-ray fluorescence spectroscopy, synchrotron X-ray powder diffraction implemented with Rietveld analysis, Fourier transform infrared spectroscopy coupled with attenuated total reflectance, Raman spectroscopy, thermogravimetric analysis coupled with differential scanning calorimetry, and high-temperature oxide melt drop solution calorimetry. Our results shed light on the formation of natural xenotimes and lay the foundation for their industrial applications as thermal coating materials.

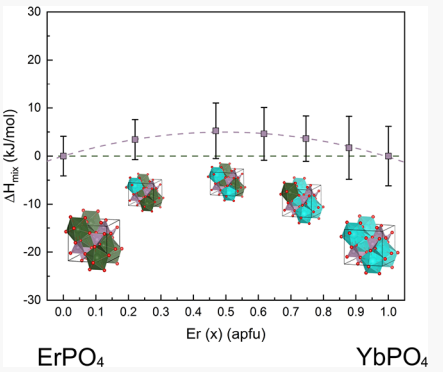

KEYWORDS: *xenotime, solid solution, enthalpy of mixing, rare earth elements, thermal barrier coating*

1. INTRODUCTION

Rare earth elements (REEs), the 15 naturally occurring lanthanides plus yttrium (Y) and scandium (Sc),[1] are ubiquitous in modern pedestrian life as they are critical components of many advanced devices and technologies. This is reflected by REEs being utilized in permanent magnets found in electric vehicles, wind turbines, and smartphones.[2] However, industrially, REEs have been important commodities for over a hundred years, being utilized in everything from gas lighting mantels to petroleum cracking catalysis.[3] The list of potential applications for REEs is ever-growing, with industries continually finding even more applications for the elements. The aerospace industry is an example that has historically used REEs in guidance systems[2] and now investigates many different types of REE-based ceramic materials as environmental barrier coatings (EBCs) to improve the efficiency of combustion engines.[4−12] It is anticipated that the demand for REEs will continue to surge, which, however, will certainly stress the overall supply of REEs. While REEs have bulk crustal abundances equal to those of other industrially important metals such as copper (Cu), zinc (Zn), or molybdenum (Mo),[2,13] they are hardly ever concentrated to economic levels. REEs are commonly subdivided into light (LREEs) and heavy (HREEs) based upon their atomic masses and radii,[13,14] as the lanthanides exhibit a systematic decrease in atomic radii with increasing atomic number (Z).[15] The LREEs consist of lanthanum (La)−europium (Eu), and HREEs consist of gadolinium (Gd)−lutetium (Lu), in addition to Y and Sc. Typically, LREEs comprise 60−90% of REE ores, whereas HREEs, which are in most industrial demand, are rarely concentrated to economic levels.[2,16,17] To date, there are only a few notable deposits (*i.e.*, Lofdal (Namibia) and Browns Range (Australia)) where HREEs can make up >80% of the total REE budget.[18−21]

In both of these deposits, xenotime ($HREEPO_4$) is an important ore mineral and globally is an economical source of HREE, which is commonly associated with other hydrothermal deposits.[22] Much of the thermodynamic properties on the xenotime endmembers have been elucidated through a combination of calorimetric methods,[23−25] solubility studies,[22,26] and high-pressure studies.[27−30] However, in natural

Received: February 19, 2022
Revised: April 19, 2022
Accepted: April 20, 2022
Published: May 2, 2022

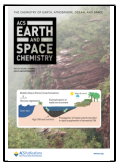

systems, endmembers are rarely observed, and instead, intermediate compositions, as a result of solid solutions, are more commonly observed. In solid solutions, the mixing behavior of HREEs in the xenotime structure ($I4_1/amd$) is paramount in modeling ore-forming processes.[31] If HREEs are mixing as ideal solutions, then no additional interaction parameter (W_x) is needed to model their thermodynamic behavior; however, if their mixing is non-ideal, then regular or subregular (or other more complex) solutions need to be employed where W_x must be included to accurately describe their mixing behavior.[32] Although W_x's of other REE phosphate minerals such as monazite ($LREEPO_4$, space group $P2_1/n$) and cheralite ($[2REE]_{(x)}[CaTh]_{(1-x)}PO_4$, space group $2/m$) have been experimentally determined by calorimetric techniques,[33−35] only a few theoretical studies[36,37] and an empirically derived estimation[31] have been conducted on the HREE xenotime.

As mentioned above, many REE-based ceramic materials are being investigated for a wide swath of applications as advanced ceramic materials. The thermophysical and thermochemical properties of xenotime make it ideal to be used as EBC or thermal barrier coating (TBC) in aerospace applications[4,38] as the material possesses a low chemical reactivity and a high melting point.[39−44] Currently, through the utilization of solid solutions, one can tailor and ultimately improve the thermophysical and thermochemical properties of EBC or TBC,[6] which is most likely a result of the entropy-driven stabilization effect.[45]

Additionally, the low chemical reactivity, low solubility, and resistance to radiation damage also make xenotime a promising ceramic waste host candidate for permanent immobilization and disposal of actinides associated with nuclear wastes.[46−51] As xenotime is isostructural to other zircon structure-type phases, including coffinite ($USiO_4$), thorite ($ThSiO_4$), and stetindite ($CeSiO_4$), they share many similar thermochemical and thermophysical properties. Xenotime also has the ability to accommodate trivalent elements, the dominant valence state of the late actinides (Am−Es),[52−54] which were predicted to be thermodynamically unstable in orthosilicates.[55−57] All of the actinide orthophosphates (Pu−Es) synthesized in the air have been reported to adopt the monazite structure,[50,52,58−61] yet there are also reports that Np and Pu were found to be stabilized in the xenotime structure ($Y_{(x)}An_{(1-x)}PO_4$, where An = Np or Pu) under reducing environments.[52] This stabilization within the xenotime structure could most likely be attributed to the favorable energetics of mixing, similar to what is found with uranothorite ($Th_{(x)}U_{(1-x)}SiO_4$).[57,62,63]

Thus, studying the crystal chemistry and thermodynamics of a xenotime solid-solution series has both fundamental and applicable significance. In this work, we report the crystal chemistry, high-temperature material behaviors, and thermodynamic stability of an Er−Yb binary xenotime solid-solution series ($Er_{(x)}Yb_{(1-x)}PO_4$) with hydrothermal origins.

2. EXPERIMENTAL METHODS

2.1. Sample Synthesis. $Er_{(x)}Yb_{(1-x)}PO_4$ were hydrothermally synthesized through the modification of a method originally reported by Mesbah *et al.*[64] for xenotime−thorite solid solutions. The following reagents were used: $Er(NO_3)_3\cdot 5H_2O$, $Yb(NO_3)_3\cdot 5H_2O$, H_3PO_4, $NaHCO_3$, NaOH, and HNO_3. The concentration of the solutions utilized was 0.05−0.3 M $Er(NO_3)_3\cdot 5H_2O$, 0.05−0.3 M $Yb(NO_3)_3\cdot 5H_2O$, and 0.05−0.3 M H_3PO_4. A 1.0 M solution of $NaHCO_3$ was prepared as a buffer, and 4−8 M NaOH solutions were used to adjust the pH to 8.7. The procedure involved pipetting stoichiometric amounts of the Er^{3+}, Yb^{3+}, and PO_4^{3-} solutions under constant stirring. The pH was then adjusted to 11−12 by dropwise addition of NaOH and subsequently buffered to 8.7 by adding $NaHCO_3$. The final solutions contained in a 23 mL Teflon line Parr autoclave were then placed in a preheated oven of 220−250 °C for 7 days followed by natural cooling to room temperature. The resulting precipitates were separated from the supernatant by centrifugation at 4000 rpm and washed four to five times with 18.2 mΩ deionized water and once with ethanol. The resulting solids were then dried overnight at 60 °C. *Safety statement: No unexpected or unusually high safety hazards were encountered.*

2.2. Total Reflection X-ray Fluorescence Spectroscopy (TXRF). A Bruker S2 PICOFOX benchtop TXRF spectrometer equipped with an air-cooled molybdenum X-ray source of 50 kV was used for the study.[65] The instrument's gain correction and resolution were calibrated prior to each series of measurements. Each measurement had an acquisition time of 120 s and was performed in triplicate with the average reported here. The spectra were processed by the Spectra 7 software using the optimized Bayes fit technique.[66] The resulting spectra are presented in Figures S1 and S2 and listed in Table S1 in the Supporting Information.

2.3. Thermogravimetric Analysis Coupled with Differential Scanning Calorimetry (TGA-DSC). The TGA-DSC measurements from 28 to 1200 °C, with a heating rate of 10 °C/min and under a flowing N_2 atmosphere (20 mL/min), were performed by a Setaram SetSYS 2400 thermogravimetric differential scanning calorimeter. The temperature and sensitivity of the instrument were calibrated by heating indium, tin, lead, zinc, and aluminum across their fusion point repeatedly at the temperature change rates of 5, 10, 15, and 20 °C/min. The calibration and methodology detailed above are described in more detail in previous reports.[55,67−69]

2.4. Vibrational Spectroscopies. Samples were characterized through a combination of FTIR and Raman spectroscopy. The FTIR spectra were recorded in the 600−4000 cm^{-1} range via a PerkinElmer FTIR Spectrum 400 device. Powder samples were deposited directly on the surface of an ATR crystal without any prior preparation and with a collection time of 30 s and five scans. The Raman spectroscopic measurements were conducted using an HR Evolution LabRAM Raman spectroscopy system equipped with both a 532 nm laser and a 785 nm laser. Each of these lasers was utilized to get a complete understanding of the normal vibrational modes associated with the $Er_{(x)}Yb_{(1-x)}PO_4$ system, as both Er^{3+} (532 nm) and Yb^{3+} (785 nm) exhibit strong laser-induced photoluminescence.[70] The laser outputs were filtered to 25−30 mW to prevent thermal damage. The total time of counting ranged from 3 to 120 s. The system is equipped with a grating of 600 g/mm, which yields an effective resolution of less than 1 cm^{-1}. For both FTIR and Raman data, band component analysis was done by means of the Peakfit function within the OriginPro 2020 software suite using a Lorentz function with the minimum number of components. The resulting fittings and deconvolutions yielded correlation coefficients R^2 greater than 0.967 and are displayed in Figures S3−S7 and reported in Tables S2−S6 in the Supporting Information.

2.5. Scanning Electron Microscopy and Energy Dispersive X-ray Spectroscopy (SEM-EDS). Scanning electron microscopy was carried out to observe the size

https://doi.org/10.1021/acsearthspacechem.2c00052
ACS Earth Space Chem. 2022, 6, 1375−1389

distribution and surface morphology by an FEI Apreo VolumeScope SEM equipped with a field emission gun electron source, backscattered electron detectors, and TEAM Pegasus integrated EDS-EBSD. All micrographs were collected under high vacuum conditions with an accelerating voltage of 20 kV, and magnifications from 50 to 40,000 times. The resulting micrographs are presented in Figures S8−S17 in the Supporting Information.

2.6. Synchrotron Powder X-ray Diffraction (XRD). Synchrotron powder X-ray diffraction was conducted at Sectors 6-ID-D and 11-ID-C of the Advanced Photon Source (APS) at Argonne National Laboratory (ANL). The wavelength of the X-ray beam was 0.123696 Å (the distance to the detector between 350 and 360 mm) and 0.1173 Å (1600 mm as the sample−detector distance), respectively, for 6-ID-D and 11-ID-C. All collected two-dimensional (2D) images were calibrated, masked, and integrated through the use of the Dioptas processing software,[71] which were then analyzed through the Rietveld method using the General Structure Analysis System software version II (GSAS-II),[72] where the instrument parameters were obtained using the CeO_2 standard. The backgrounds were modeled by the Chebyshev function with 6−20 coefficients. The above Rietveld refinement procedures are also stated previously elsewhere.[67,73−77]

2.7. High-Temperature Oxide Melt Solution Calorimetry. The enthalpies of the drop solution (ΔH_{ds}) were directly measured by a Setaram AlexSYS-1000 Calvet-type calorimeter. The calibration of the instrument was conducted by performing transpose temperature drops using solid pieces of α-Al_2O_3 and Pt. Powdered samples were hand pressed into pellets, with masses between 1.211 and 5.217 mg, and dropped from room temperature into a molten solvent of sodium molybdate ($Na_2O{\cdot}MoO_3$) contained in a Pt crucible at 700 °C. The calorimeter chambers were continuously flushed with O_2 gas at a rate of ∼110 mL/min to facilitate a constant gas environment above the solvent. The flushing of O_2 gas above the solvent also further aids in maintaining an oxidative solvent environment by oxidizing any low-valence Mo to Mo^{+6}. All of the calibration and methodology employed in this study are further described in more detail in previous reports.[55,56,67,73,78−82]

3. RESULTS

3.1. Thermogravimetric Analysis Coupled with Differential Scanning Calorimetry (TGA-DSC). TGA-DSC experiments (Figure 1) revealed that the samples have good thermal stability up to 1200 °C under an inert N_2 atmosphere. A long mass loss (∼4.2%) was identified from 50 to 1000 °C, which could correspond to the removal of absorbed and confined molecular water (in the [001] channel of the xenotime structure), as well as hydroxyl species due to its endothermic nature. Such an attenuated or "sluggish" dehydration and dehydroxylation of other zircon-type materials have been previously reported and discussed in the works by Strzelecki *et al.*[74] Further details on the dehydration and dehydroxylation are discussed in later sections.

3.2. Synchrotron Powder X-ray Diffraction (XRD). The diffraction patterns of the pristine samples confirmed a single-phased orthophosphate ($I4_1/amd$) with no observed impurities or chemical inhomogeneities (Figure S18). We performed Rietveld refinements based on the structural models reported by Ni *et al.*[83] for $ErPO_4$ and $YbPO_4$. The occupancy of the MO_8 site in $Er_{(x)}Yb_{(1-x)}PO_4$ was fixed to the compositions determined by TXRF. The resulting refinements yielded R_{wp} values ranging from 2.65 to 8.34%. The pristine xenotime phases are nanocrystalline, with sizes ranging from 15 to 70 nm.[84−89] Samples recovered after the TGA-DSC to 1200 °C have additional non-xenotime diffraction peaks (Figure S19), which point to Er−Yb sesquioxide solid-solution phases ($Er_{(2x)}Yb_{(2-2x)}O_3$) that are isostructural to bixbyite ($Ia3$).[90] As xenotime has been found to be thermally stable to over 1600 °C till melting,[39] the observation of $Er_{(2x)}Yb_{(2-2x)}O_3$ implies that there could be amorphous $Er_{(2x)}Yb_{(2-2x)}O_3$ in the pristine samples, similar to what have been found in the hydrothermally synthesized uranothorite.[91] Confirmation of these requires high-temperature XRD or X-ray absorption spectroscopic measurements, which we intend to perform in the future.

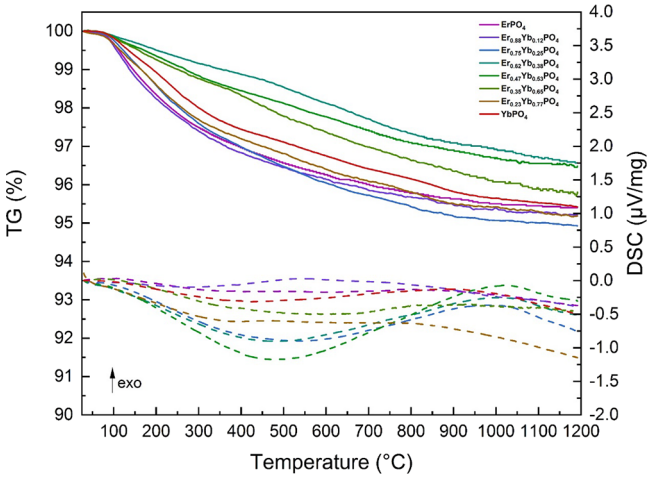

Figure 1. TG and DSC of $Er_{(x)}Yb_{(1-x)}PO_4$ up to 1200 °C, respectively, plotted in solid and dashed curves.

The refined unit cell parameters of pristine and thermally treated $Er_{(x)}Yb_{(1-x)}PO_4$ (listed in Tables S7 and S8 and plotted in Figure 2) decrease almost linearly as a function of x following Vegard's law. However, both the unit cell volume and the a-parameter of all compositions significantly decrease after being thermally treated to 1200 °C. By contrast, the c-parameter increases for some compositions but decreases for others. Causes of the change in unit cell parameters before and after the thermal treatment will be discussed in the succeeding sections.

3.3. Vibrational Spectroscopies. The FTIR spectra were recorded for the pristine (Figure 3a) and thermally treated samples (Figure 3b). The spectra of the pristine samples could be separated into three distinct zones of interest: 600−1300, 1300−2000, and 2500−4000 cm^{-1}. The spectra of those collected after TGA-DSC to 1200 °C only had one distinct zone of interest (the first zone, 600−1300 cm^{-1}). Being isostructural to zircon, xenotime shares similar vibrational behaviors and band assignments, which have been reported by Nasdala *et al.*[92] and Dawson *et al.*[93] for zircon. The $I4_1/amd$ space group has seven active FTIR vibrational modes, which were determined through a factor-group analysis.[93,94] These vibrational modes can be assigned to the internal and external vibrations of the PO_4 tetrahedron. Of the seven vibrational modes, four ($\Gamma_{int} = 2A_{2u} + 2_{Eu}$) can be assigned to internal vibrational modes and three ($\Gamma_{ext} = A_{2u} + 2_{Eu}$) to external vibrational modes. The vibrations observed within 600−1300 cm^{-1} correspond to the internal vibrational modes of the PO_4 tetrahedron. Note that a wide massif was systematically

https://doi.org/10.1021/acsearthspacechem.2c00052
ACS Earth Space Chem. 2022, 6, 1375−1389

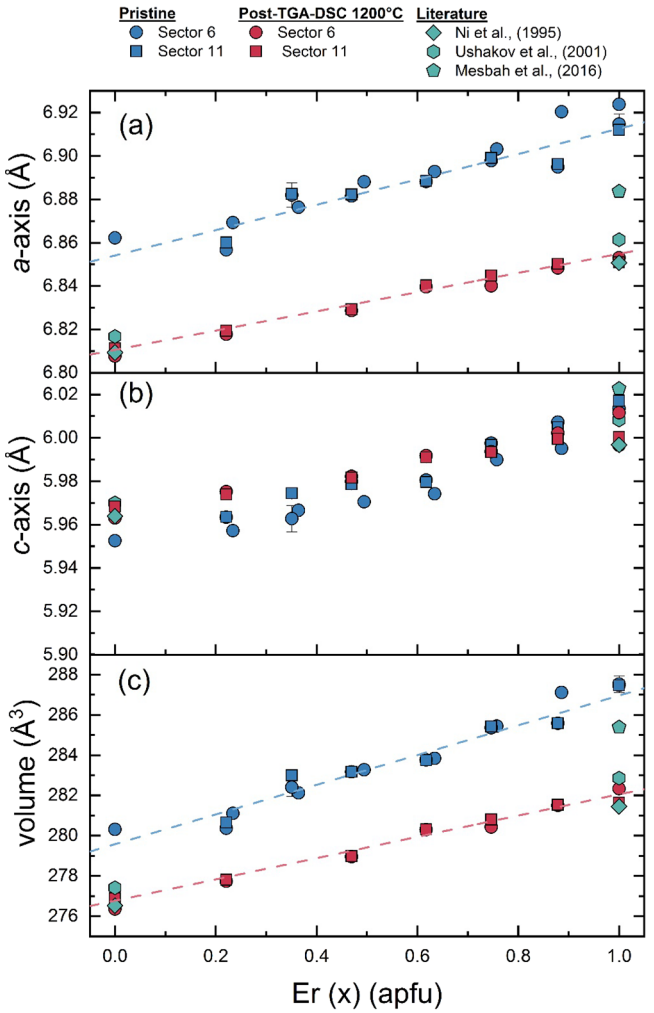

Figure 2. Variation of unit cell parameters of $Er_{(x)}Yb_{(1-x)}PO_4$ as a function of Er content. Blue symbols (a–c) indicate data points of the pristine samples, red symbols indicate date collected on the samples recovered after TGA-DSC, and green symbols indicate literature values.[25,64,83] The data represented with circles were collected at beamline 6 ID-D, and those represented with squares were collected at beamline 11 ID-C.

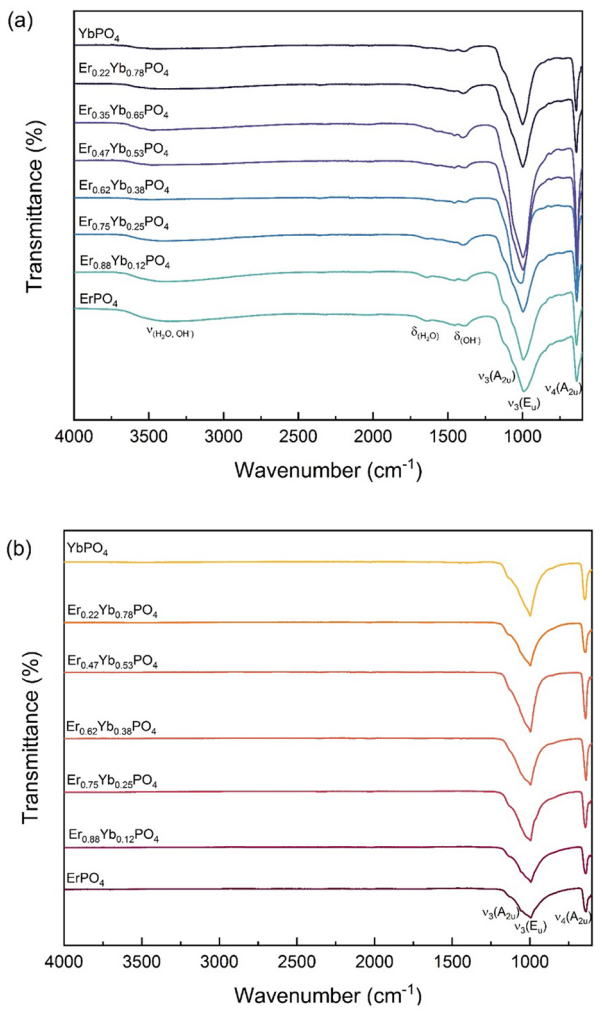

Figure 3. FTIR spectra of $Er_{(x)}Yb_{(1-x)}PO_4$: (a) pristine and (b) after TGA-DSC experiments to 1200 °C.

recorded between 700 and 1200 cm^{-1}, similar to what was found in Clavier *et al.*,[95] which makes it difficult to unambiguously differentiate the components assigned to symmetric and antisymmetric stretching vibrations. As only the antisymmetric internal motions of the PO_4 tetrahedron are visible by IR, this would mean that the doubly degenerate antisymmetric stretching mode (ν_3–E_u) is around 998 cm^{-1}, while the antisymmetric stretching mode (ν_3–A_{2u}) would be around 1125 cm^{-1}. The sharp band centered around 639 cm^{-1} corresponds to the antisymmetric deformation mode (ν_4–A_{2u}). Then, the doubly degenerate antisymmetric deformation mode (ν_4–E_u) and the three external vibrational modes (Γ_{ext} = A_{2u} + 2_{Eu}) could not be observed as they would appear below 600 cm^{-1}.

The vibrational bands occurring in 1300–2000 and 2500–4000 cm^{-1} are indicative of hydration and hydroxylation, which only appear in the pristine samples. Three relatively sharp vibration bands were observed, with the first corresponding to the deformation band of hydroxyl (OH^-) groups located near 1300 cm^{-1}, the second located near 1400 cm^{-1} for the stretching mode of CO_2, and the third near 1600 cm^{-1} for the deformation band of molecular water. Lastly, a large broad band in high wavenumbers (~3500 cm^{-1}) corresponds to the stretching modes of both hydroxy groups and molecular water.[96–98]

For Raman spectroscopy, the $I4_1/amd$ space group has 12 active Raman vibrational modes belonging to the D_{4h} point group.[93,94,99] Seven (Γ_{int} = $2A_{1g}$ + $2B_{1g}$ + B_{2g} + $2E_g$)[93,99] can be assigned to the internal vibrations of the PO_4 tetrahedron, while the remaining five (Γ_{int} = $2B_{1g}$ + $3E_g$)[93,99] can be assigned to the external vibrations of the PO_4 tetrahedrons.[93,99,100] Due to the interaction of the PO_4 tetrahedra with the MO_8 dodecahedra, the tetrahedra cannot be considered as strictly independent units,[101] and so there are no reported spectra with all 12 active Raman modes for zircon-type phases.[94] All the spectra from the two lasers are separated into two distinct zones of interest (Figure 4): 900–1200 and 100–900 cm^{-1}. First, P–O stretching motions are observed and assigned as the symmetric stretching (ν_1–A_{1g}) occurring around 1005 cm^{-1}, the anti-symmetric stretching (ν_3–B_{2g}) occurring around 1065 cm^{-1}, and the doubly degenerate anti-symmetric stretching (ν_3–E_g) occurring around 1029 cm^{-1}. The second zone contains the internal bending motions of the PO_4 tetrahedron and the lattice or external motions of the PO_4 tetrahedron. In addition, the second zone has the majority of

https://doi.org/10.1021/acsearthspacechem.2c00052
ACS Earth Space Chem. 2022, 6, 1375–1389

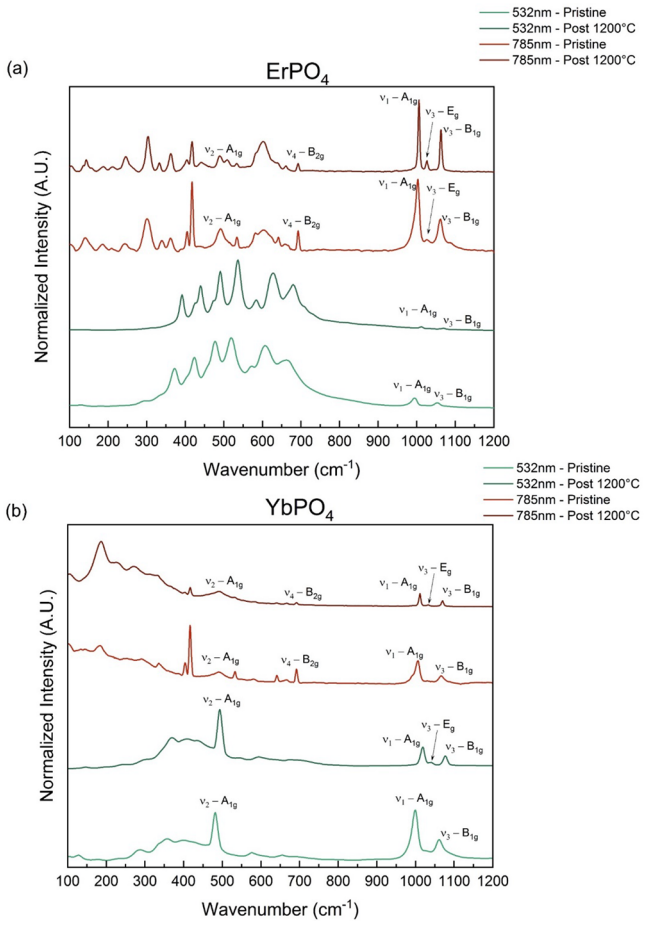

Figure 4. Raman spectra collected with 532 and 785 nm lasers for (a) $ErPO_4$ and (b) $YbPO_4$.

Er^{3+} and Yb^{3+} photoluminescence, observed when using the 532 and 785 nm laser, respectively. However, several of the bands were able to be assigned as the symmetric bending (ν_2−A_{1g}) occurring around 492 cm^{-1} and the anti-symmetric bending (ν_4−B_{2g}) occurring around 692 cm^{-1}. The spectra and peak positions are in excellent agreement with those of $ErPO_4$ and $YbPO_4$ previously reported by Begun *et al.*[102]

3.4. High-Temperature Oxide Melt Drop Solution Calorimetry. The standard enthalpy of formation (ΔH°_f) and enthalpy of formation from oxides ($\Delta H_{f,\,ox}$) were determined for $Er_{(x)}Yb_{(1-x)}PO_4$ by high-temperature oxide melt drop solution calorimetry in the $Na_2O{\cdot}MoO_3$ solvent. Prior to calorimetry, samples were calcinated at 1200 °C to remove hydrous species (absorbed molecular water, confined molecular water, and hydroxyl groups). Trace amounts of RE_2O_3 impurity (identified by XRD, Table S9) were corrected in the thermochemical cycles. The experimentally determined ΔH_{ds} as a function of erbium content x is plotted in Figure 5a and tabulated in Table S10. The variation in ΔH_{ds} was fitted by eq 1 and suggests a negative deviation from thermodynamic ideality.

$$\Delta H_{ds} = a + bx + cx^2 \quad (1)$$

where a = 145.66 ± 0.13 kJ/mol, b = −18.23 ± 0.69 kJ/mol, c = 20.19 ± 0.72 kJ/mol, and adjusted R^2 = 0.995. The determined enthalpies of formation from oxides ($\Delta H_{f,ox}$) and elements (ΔH°_f) at room temperature (Table 1) were calculated through the thermochemical cycles in accordance with Hess's law (Table S11). Note that $\Delta H_{f,ox}$ of $ErPO_4$ (−282.35 ± 4.74 kJ/mol) and $YbPO_4$ (−277.20 ± 3.73) obtained from this work agree in general with the previous values reported in Ushakov *et al.* for $ErPO_4$ (−275.6 ± 1.9 kJ/mol) and $YbPO_4$ (−269.6 ± 2.4 kJ/mol).[25]

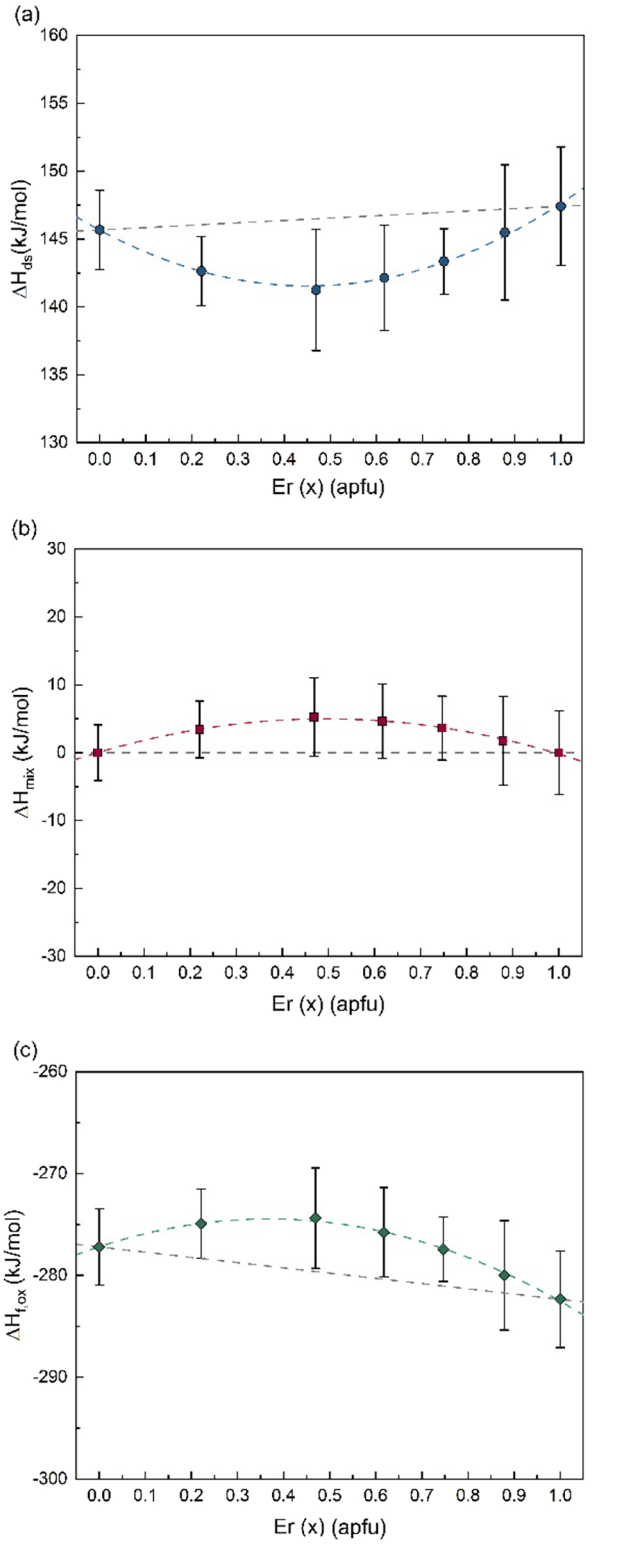

Figure 5. (a) Enthalpies of the drop solution; (b) enthalpies of mixing, fitted by $\Delta H_{mix} = 20.3x(1 - x)$; and (c) enthalpies of the formation of $Er_{(x)}Yb_{(1-x)}PO_4$ from their binary oxides at 25 °C as a function of Er content.

https://doi.org/10.1021/acsearthspacechem.2c00052
ACS Earth Space Chem. 2022, 6, 1375−1389

Table 1. Enthalpies of the Formation of $Er_{(x)}Yb_{(1-x)}PO_4$ from Binary Oxides and Elements

formula	$\Delta H_{f,ox}$ (kJ/mol)	ΔH°_f (kJ/mol)
$ErPO_4$	−282.4 ± 4.7	−1984.8 ± 6.6
$Er_{0.88}Yb_{0.22}PO_4$	−280.0 ± 5.4	−1977.3 ± 5.3
$Er_{0.75}Yb_{0.25}PO_4$	−277.4 ± 3.2	−1969.1 ± 4.9
$Er_{0.62}Yb_{0.38}PO_4$	−275.8 ± 4.4	−1961.9 ± 4.9
$Er_{0.47}Yb_{0.53}PO_4$	−274.4 ± 4.9	−1954.2 ± 5.0
$Er_{0.22}Yb_{0.78}PO_4$	−274.9 ± 3.4	−1944.1 ± 4.7
$YbPO_4$	−277.2 ± 3.7	−1936.9 ± 5.7

4. DISCUSSION

4.1. Role of Water/Hydroxyl in the Xenotime Structure. The mass losses observed in TGA from 50 to 1000 °C are interpreted to be a combination of the breakdown of hydroxylated phosphate tetrahedrons $(PO_{4-x}(OH)_x)$, similar to what has been observed in zircon[96,103] and coffinite.[74] The release of confined molecular water within the [001] channels in the xenotime structure has also been seen for coffinite[104] and stetindite.[74] This is also supported by the determined unit cell parameters of samples before and after thermal treatment (Figure 2). The unit cell volume has a significant decrease (1.5 ± 0.2%) after being heated to 1200 °C, which agrees extremely well with those of the endmembers previously reported by Ushakov *et al.*[25] and Ni *et al.*,[83] who used flux-grown crystals that were completely anhydrous.

The reduction in the unit cell volume is mainly a result of the decrease in the *a* axis (Figure 2a) or, more precisely, the contraction along the (001) plane. Since the channels along the *c* axis contain water, the removal of water upon heating causes the contraction of the structure parallel to (001). This further collaborates with the original hypothesis of Janeczek[104] and later confirmation by Strzelecki *et al.*[74] Kijkowska also observed a prolonged mass loss via TGA-DSC for hydrothermally prepared xenotimes and sequent contractions of the unit cell parameters on the sample recovered afterward,[105] which, however, were hypothesized to be related to zeolitic water. In regard to the *c* axis, there was no systematic trend before and after thermal treatments (Figure 2b). This may be because of the cancellation of hydrated and hydroxylated effects, the latter of which yields a shorter unit cell axis than one without.[74,103] Our vibrational spectroscopy results collaborate with all previous assertions. FTIR spectra indicate that the pristine samples are clearly both hydrated and hydroxylated (Figure 3a), whereas post-TGA samples are completely anhydrous. From Raman spectra, the positions of the ν_1 and ν_3 vibrational bands move to higher wavenumbers after being calcined (Figure 6), which indicate the decrease in P−O bond length upon calcination and implies the removal of the confined [001] water.[103] Again, this is in excellent agreement with observations by Strzelecki *et al.*[74] on $CeSiO_4$, where the ν_1 and ν_3 vibrational bands shift to higher wavenumbers using *in situ* high-temperature Raman spectroscopy.

These results have important implications for the descriptive mineralogy and geologic history of REE deposits, as vibrational spectroscopic techniques become more prevalent in geologic laboratories.[106−108] For instance, Clavier *et al.*[95] proposed a schematic methodology for categorizing lanthanide phosphate polymorphs through vibrational spectroscopy besides the common diffraction techniques (*e.g.*, X-ray, neutron, electron diffraction). For example, to discern xenotime from the

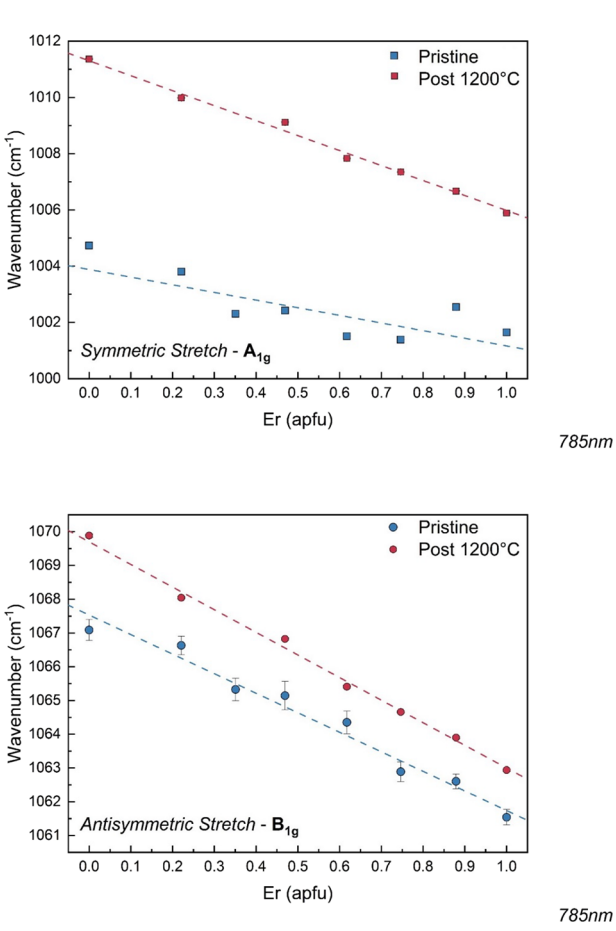

Figure 6. Variation in the frequencies of P−O stretching modes of $Er_{(x)}Yb_{(1-x)}PO_4$ as a function of Er content.

hydrous HREE phosphate mineral churchite ($HREEPO_4 \cdot 2H_2O$, space group *C*2/*c*), one would observe if there are vibrational bands between 1500 and 1600 cm^{-1} in FTIR spectra since bending motions of H_2O only clearly present in churchite but not xenotime. This method has been used by Zhukova *et al.* to discern the mineralogy of the Mount Weld REE supergene deposit in Australia.[109] However, as demonstrated above, all of the pristine hydrothermally prepared xenotime samples have the deformation modes of H_2O between 1500 and 1600 cm^{-1} in the FTIR spectra with small intensities. This observation does not undermine the use of the vibrational spectroscopy-based methodology for tracing the geologic conditions but suggests a more careful examination of the origin of mineral samples. Xenotime typically forms as a primary accessory mineral in igneous and metamorphic (*i.e.*, granites and schist) rocks at elevated temperatures,[110,111] whereas churchite forms as a secondary trace mineral as a weathering product (*i.e.*, laterites) under much lower temperatures,[112,113] which is even reflected in the synthetic conditions of producing churchite.[114] Thus, the identification of these minerals has a profound influence on interpreting the geologic history of a given lithology. If vibrational spectroscopy alone is to be used to discern the proper identification of which $HREEPO_4$ phase is present, the deformation bands associated with the bending motions of the P−O in both IR and Raman are much more indicative of elucidating if the phase is xenotime or churchite. This is due to the absence of the symmetric bending motions in IR spectra of

https://doi.org/10.1021/acsearthspacechem.2c00052
ACS Earth Space Chem. 2022, 6, 1375−1389

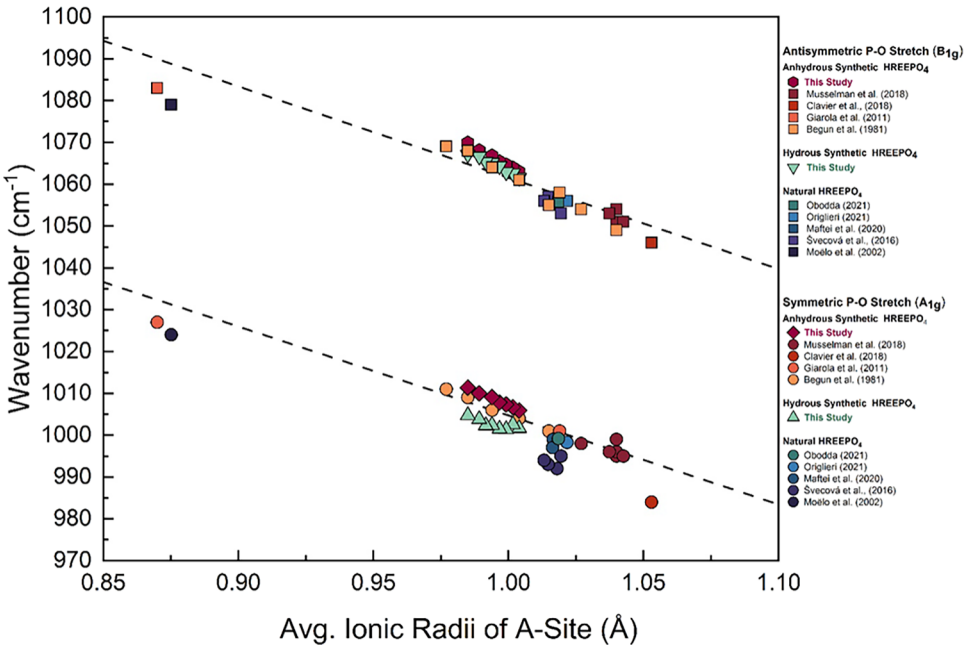

Figure 7. Variation in the frequencies of symmetric (A_{1g}) and antisymmetric (B_{1g}) stretching modes of synthetic and natural xenotimes versus the average ionic radii of the A-site cation, assuming an eightfold coordination by oxygen.[15,95,102,116−121]

xenotime, as discussed above. Lastly, one should always perform additional diffraction examinations to differentiate phosphate phases.

4.2. Thermodynamics of Xenotime Solid Solutions with Implications for Their Mineralization. When looking at the size distribution of the ionic radii of the HREEs within the xenotime structure ($^{VIII}r_{HREE^{3+}}$), the average size is 1.008 Å, closest to that of Er^{3+} (1.004 Å). The maximum difference in ionic radii exhibited by the HREEs in the xenotime structure is 6.25% (Tb and Lu), while the average difference in the size of the ionic radii is 2.0%, approximately that of Er^{3+} and Yb^{3+} (1.9%). On the other hand, naturally occurring xenotime is dominated by Y^{3+}, which reflects that it has the highest overall geochemical abundance of any HREE.[115] The difference in size between Y^{3+} and other HREEs is 1.8%, also approximately that of Er^{3+} and Yb^{3+} (1.9%). This is demonstrated when plotting the variation in the positions of the symmetric (A_{1g}) and antisymmetric (B_{1g}) stretches reported in a suite of synthetic and natural xenotimes (Figure 7).[15,95,102,116−121] Here one can observe that both synthetic and natural samples follow a nearly linear dependency of the average ionic radii of the A-site, assuming metals to be eightfold coordinated. The only observed deviations are associated with symmetric (A_{1g}) stretches reported by Švecová *et al.* for the natural xenotimes, which may be due to the samples being both hydrothermally altered and metamict.[118] Details of Raman peak positions of synthetic and natural xenotimes are reported in the Supporting Information (Table S12).[15,95,102,116−121] Therefore, the $ErPO_4$-$YbPO_4$ solid-solution system is an ideal analogue system in understanding the thermodynamic mixing behavior of HREEs in natural xenotime systems.

The results of the XRD (and Raman) indicate that the mixing of Er and Yb in $Er_{(x)}Yb_{(1-x)}PO_4$ follows Vegard's law, as their unit cell parameters have a nearly linear dependency as a function of x. This would imply that a regular solution model should be employed effectively to evaluate the thermodynamics of cationic mixing in the $ErPO_4$-$YbPO_4$ solid solution. In accordance with the regular solution model, the Gibbs free energy of mixing can be calculated as follows:

$$\Delta G_{mix} = \Delta H_{mix} - T\Delta S_{mix} \quad (2)$$

where both the enthalpy of mixing (ΔH_{mix}) and the entropy of mixing (ΔS_{mix}) are needed. As the regular solution model is being used, ΔH_{mix} can then be expressed by using the interaction parameter (W_x):

$$\Delta H_{mix} = W_x \cdot x \cdot (1 - x) \quad (3)$$

Here we evaluated W_x experimentally by calorimetry, which has been previously demonstrated in solid-solution systems.[45,57,122−127] ΔH_{mix} can be derived from the measured ΔH_{ds} by the equation $\Delta H_{mix} = -\Delta H_{ds}(Er_{(x)}Yb_{(1-x)}PO_4) + x\Delta H_{ds}(ErPO_4) + (1-x)\Delta H_{ds}(YbPO_4)$. The derived heats of mixing (Figure 5b) show a deviation from the ideal mixing toward the endothermic direction, suggesting that the intermediate compositions are slightly enthalpically unstable compared to a mixture of the two endmembers. Using eq 3, the interaction parameter can be obtained to be $W_x = 20.3 \pm 0.8$ kJ/mol, suggesting that the solid solution is enthalpically not favorable to form (Figure 8a). Note that the calorimetrically determined W_x value includes two contributions: (1) the elastic term that originates from the volume of mixing due to mismatch of sizes and (2) the chemical term considering bonding and local mixing features.[63,128] The elastic contribution of W_x can be empirically approximated based on the unit cell volume and Young's modulus, which has been used by Migdisov *et al.*[31] to estimate the heats of mixing of HREE xenotimes:

$$W_x = \bar{E}\left(\frac{\Delta V^2}{6V}\right) \quad (4)$$

where $\bar{E}$ is the average Young's modulus of all REE xenotime endmembers (168.8 GPa)[31] and ΔV is the difference between the molar volumes of the two endmembers, 42.453 ± 0.009 cm^3/mol for $ErPO_4$ and 41.646 ± 0.005 cm^3/mol for $YbPO_4$,

https://doi.org/10.1021/acsearthspacechem.2c00052
ACS Earth Space Chem. 2022, 6, 1375−1389

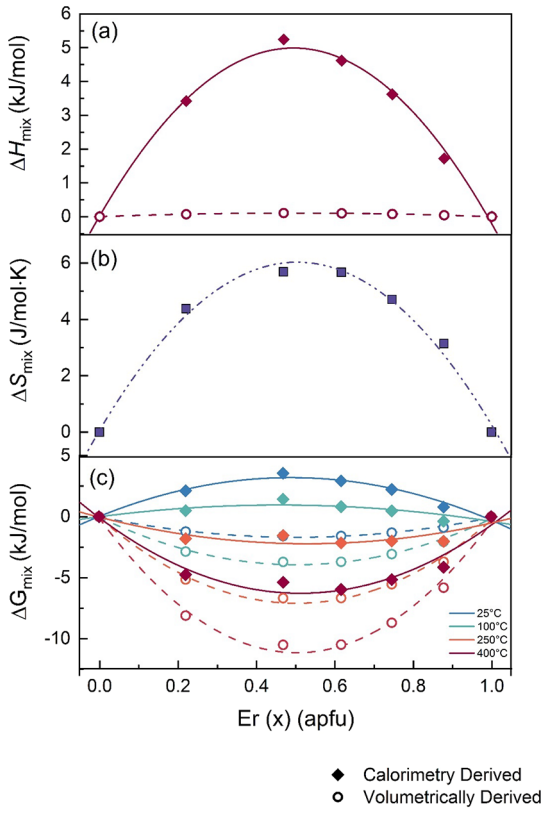

Figure 8. (a) Enthalpies of mixing, (b) entropies of mixing, and (c) Gibbs free energy of mixing of $Er_{(x)}Yb_{(1-x)}PO_4$ as a function of Er content. Open circles and dashed lines represent the volumetrically derived ΔH_{mix}, whereas closed diamonds and solid lines represent the calorimetry derived ΔH_{mix}.

both experimentally determined from XRD (Table S6). Using these values and eq 4, the elastic W_x term was thus volumetrically derived to be 0.4 kJ/mol.

Glynn[129] proposed that for a solid-solution system to be thermodynamically stable, the interaction parameter needs to be constrained by $W/(K_BT) < 2$, which then transforms to $W <$ 5 kJ/mol at ambient conditions.[31,129] Regarding the calorimetrically determined W_x, one would expect exsolution or phase separation to occur due to a possible miscibility gap between $ErPO_4$ and $YbPO_4$. Only considering the elastic term that is volumetrically derived would predict a full solid solution across the whole composition. Such difference emphasizes the importance of performing calorimetric measurement to obtain the total enthalpy of mixing that includes both elastic and chemical effects, which thus reliably and accurately accounts for the non-ideal mixing effect.

We derive ΔS_{mix} from both the configurational entropy of mixing ($\Delta S_{mix,config}$) and vibration entropy of mixing ($\Delta S^\circ_{mix,vib}$) of Er^{3+} and Yb^{3+} in the MO_8 dodecahedron site at room temperature. The configurational term can be calculated using the Boltzmann entropy formula, as follows:

$$\Delta S_{mix,config} = -R\cdot[(1-x)\cdot\ln(1-x) + x\cdot\ln(x)] \quad (5)$$

whereas the $\Delta S^\circ_{mix,vib}$ was estimated by using an empirical relation of the standard entropy of formation ($S^\circ_{298\ K}$) to the molar volume (V_m) of a compound.[130,131] Typically, the linear equations presented in Jenkins and Glasser are used to calculate $S^\circ_{298\ K}$.[45,67,73,132] However, large discrepancies between the experimentally derived values of $S^\circ_{298\ K}$ for phosphate minerals[22−24,133−135] were found when applying these equations. Therefore, we derived our own empirical relation of standard $S^\circ_{298\ K}$ and V_m for phosphate minerals that minimizes the discrepancies between the experimentally derived values of $S^\circ_{298\ K}$[22−24,133−135] (Table S11, Figures S20 and S21).[23,25,62,133,136−155] This empirical relation is represented by the following equation,

$$S^\circ_{298\ K} = k\cdot(V_m) + c \quad (6)$$

where coefficient k is 2.46 ± 0.03 /J K^{-1} mol^{-1} and c is 5.79 ± 7.03 /J K^{-1} mol^{-1}, and V_m is the experimentally obtained molar volume (cm^3) of $Er_{(x)}Yb_{(1-x)}PO_4$. This value largely reflects the change in the vibrational entropy based on the volumetric change of the unit cell. The calculated $S^\circ_{298\ K}$ of $Er_{(x)}Yb_{(1-x)}PO_4$ is presented in Table S14. By calculating the difference between the $S^\circ_{298\ K}$ of $Er_{(x)}Yb_{(1-x)}PO_4$ and endmembers ($ErPO_4$ and $YbPO_4$), an approximated $\Delta S^\circ_{mix,vib}$ was extracted and combined with the configurational $\Delta S_{mix,config}$ to yield an estimate for ΔS_{mix} (Figure 8b). Using all this information, ΔG_{mix} values at 25, 100, 250, and 400 °C were obtained (Tables S15 and S16) and plotted in Figure 8c. These elevated temperatures were selected based on relevant geochemical conditions, such as fluid inclusion homogenization temperatures, reported for known REE deposits.[19,156−159]

While the determined ΔH_{mix} are endothermic and thus enthalpically unfavorable, the overall ΔG_{mix} values are exothermic at elevated temperatures (Figure 8c). Particularly, using the calorimetry derived W_x, ΔG_{mix} values are only positive at temperatures below 250 °C, implying a miscibility gap between Er- and Yb-rich xenotimes. This gap should shrink on increasing temperature due to the increasingly dominating effect from ΔS_{mix}. As stated earlier, the $ErPO_4$-$YbPO_4$ solid-solution system is an ideal analogue system to understand the mixing behavior of HREE; this then further indicates that ΔS_{mix} may be the major driving force and enthalpy a secondary role for HREE mixing in xenotimes. This result is reasonable because HREEs have their 4f electrons more deeply shielded due to lanthanide contraction, and thus, their bonding is dominantly ionic. A similar entropy-driven stabilization for mixing REEs has been seen in a thermodynamic study of a (La,Nd) hydroxylbastnäsite solid solution.[45] Furthermore, it is interesting to compare our result on mixing of HREEs in xenotime with mixing of early actinides (Th and U) in an isostructural system (zircon), the latter of which shows a strong influence on the thermodynamics of mixing from ΔH_{mix} rather than ΔS_{mix} that originated from the relatively stronger covalent characters of actinides.[57,63] We then can conclude that mixing HREEs in xenotime, described by a regular solution model, is close to ideal due to the largely pure ionicity, which may be deviated more from ideality when early actinides and/or LREEs are presented for mixing (*i.e.*, $HREE_{(x)}An_{(1-x)}PO_4$, where An = Th, U, Np, or Pu).

These findings have important implications to the fractionation of HREEs in phosphate ore bodies. As stated previously, REEs have a gradual systematic change in their chemical properties from LREEs to HREEs; however, there are some processes that can fractionate the REEs: either (1) LREEs from HREEs or (2) individual REEs. One mechanism to fractionate the LREEs from the HREEs is by the crystallographic constraints of the orthophosphates.[36,83,160] This is demonstrated by LREEs, with larger ionic radii, crystallizing into the monazite structure that has large nine-coordinated metal polyhedral sites, whereas HREEs, with

https://doi.org/10.1021/acsearthspacechem.2c00052
ACS Earth Space Chem. 2022, 6, 1375−1389

smaller ionic radii, crystallize into the xenotime structure in an eightfold coordination environment. Another mechanism for REE fractionation relies on the difference in the thermodynamic stabilities of REE−chloride aqueous complexes under hydrothermal conditions, where LREE−chloride complexes are more stable than HREE−chloride complexes.[31,134,161−166] If a REE−chloride hydrothermal fluid comes into contact with a phosphate source such as apatite, $Ca_{10}(PO_4)_6(OH,Cl,F)_2$, this difference in the stabilities would cause LREE−chlorides to be more mobile and be deposited distal to the fluid source as monazite, while, in opposition, HREE−chlorides begin to precipitate out of the aqueous system as xenotime. Such REE fractionation was predicted by the models of Migdisov *et al.*[31] and demonstrated by the experimental work of Strzelecki *et al.*[167]

On top of the crystallographic and aqueous thermodynamic mechanisms, this study emphasized another cause for fractionation, which is the non-ideal thermodynamics in the solid-solution phases that are attributed to majorly entropic and minorly enthalpic effects. The non-ideality controlled by W_x can lead to the separation of neighboring HREE into different xenotime endmembers. However, one should not overestimate such enthalpic effect in natural systems, where often multiple HREEs are mixing in xenotime and attenuate the non-ideal effect because of high entropy. Thus, a reliable W_x (*e.g.*, measured by calorimetry) can ensure the accurate generation of a solid-solution model, which will be combined with thermodynamic descriptions of aqueous phases for the correct prediction of mineralization and fractionation of REEs under relevant geochemical conditions.

4.3. High-Temperature Thermochemistry of $Er_{(x)}Yb_{(1-x)}PO_4$. With the increasing interest in using $HREEPO_4$ for various high-temperature applications, such as a topcoat for EBC in the aerospace industry,[38] it is necessary to understand the bulk thermochemistry of $HREEPO_4$ phases at high temperatures. Here we calculated other thermodynamic parameters of $Er_{(x)}Yb_{(1-x)}PO_4$ to evaluate their suitability for such applications. First, it is paramount to determine the heat capacity (C_p), the function of which will yield temperature-dependent enthalpy and entropy terms of a given phase:

$$\Delta H_T = \Delta H_{298} + \int_{298}^{T} C_p dT \tag{7}$$

$$\Delta S_T = \Delta S_{298} + \int_{298}^{T} \frac{C_p}{T} dT \tag{8}$$

Although C_p of both $ErPO_4$ and $YbPO_4$ have been determined experimentally by various calorimetric techniques,[24,26,42,43] C_p of intermediate compositions are not available. We estimated the C_p of the intermediate compositions by employing the Neumann−Kopp rule, which relies on the summation of known C_p of its constituent binary oxides.[168] The derived C_p[133,169] (Table S17) are in good agreement with the previously reported data for $ErPO_4$ and $YbPO_4$ (Figure S22).[24,26,42,43] ΔH_T and ΔS_T can then be calculated and combined to derive ΔG_T for each composition for the following potential reaction of interest to the aeronautical industry: $Er_xYb_{1-x}PO_{4(solid)} + 3H_2O_{(gas)} \rightarrow Er_xYb_{1-x}(OH)_{3(gas)} + H_3PO_{4(gas)}$. However, due to the lack of gas-phase thermodynamic data of H_3PO_4 at high temperatures, the thermochemistry of the above reaction cannot be assessed. Therefore, we performed a thermochemical evaluation of just the $Er_{(x)}Yb_{(1-x)}PO_4$ solid-solution phase up to 727 °C (or 1000 K), with their detailed thermodynamic parameters deposited in the electronic supplement (Tables S18−S22). As the temperature increases, the effects of the positive entropy of mixing become increasingly more obvious to the point that, at the highest temperature investigated (727 °C), an overall deviation of the composition-dependent ΔG_f toward the exothermic direction begins to emerge (Figure 9). The maximum of the negative curvature is at the composition where the concentration of Er is nearly equal to that of Yb. This implies that the entropy of mixing in the $Er_{(x)}Yb_{(1-x)}PO_4$ solid solution can further enhance its thermal stability with respect to the two endmembers.

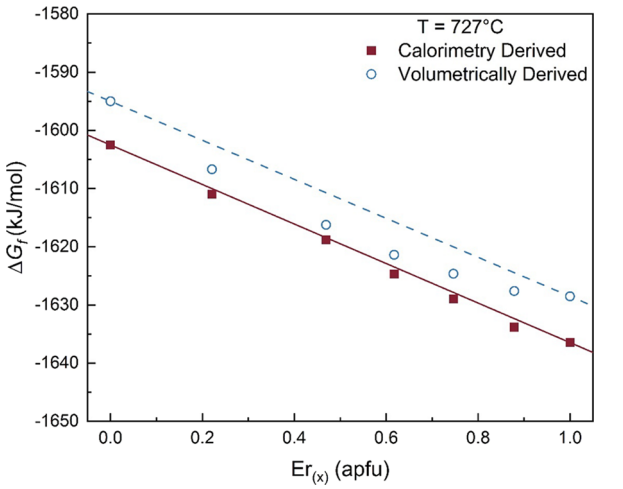

Figure 9. Predicted free energies of formation (ΔG_f) of $Er_{(x)}Yb_{(1-x)}PO_4$ at 727 °C as a function of Er content. Open circles represent the volumetrically derived ΔH_{mix}, whereas the closed squares represent the calorimetry derived ΔH_{mix}.

Thus, from an application point of view, if $Er_{(x)}Yb_{(1-x)}PO_4$ is used as an EBC material, one should synthesize the material that realizes an equal molar of Er and Yb. Furthermore, to further increase the favorable entropy of mixing and ultimately improve the thermal stability, multiple HREEs in nearly equal molar quantities would be recommended. Ideally, the selected HREEs should be chosen so that the differences are minimized for their ionic radii and thus the steric effect. For instance, mixing of equal molar portions of Y, Ho, Er, Tm, and Yb (the maximum difference in cation radii is only 3.4%) will generate a configurational entropy of 14.4 J/mol·K (using eq 5) to benefit thermal stability that scales up with temperature. Recent work by Zhao *et al.* applied such a high-entropy concept to $LREEPO_4$-monazite, with promising results.[170] The advantage of the $HREEPO_4$-xenotime system over the $LREEPO_4$-monazite system is that the predicted W_x of HREE is smaller than that for the LREE.[31] From a manufacturing and processing perspective, this would lead to more predictable phases being able to be produced, as there would be less likelihood for developing nanodomains or exsolution.[171] Overall, these observations support the concept for high-entropy oxides,[172] similar to their alloy counterparts that make use of the entropy of mixing to develop materials with superior high-temperature stability.[173]

https://doi.org/10.1021/acsearthspacechem.2c00052
ACS Earth Space Chem. 2022, 6, 1375−1389

5. CONCLUSIONS

The crystal chemistry and thermodynamic properties of a binary $ErPO_4$-$YbPO_4$ xenotime solid-solution series have been investigated using a suite of techniques, including X-ray fluorescence spectrometry, synchrotron X-ray powder diffraction implemented with Rietveld analysis, Fourier transform infrared spectroscopy coupled with attenuated total reflectance, Raman spectroscopy, thermogravimetric analysis coupled with differential scanning calorimetry, and high-temperature oxide melt drop solution calorimetry. We found that water plays a significant role in unit cell dimensions of the xenotime phases when prepared or originated hydrothermally. Furthermore, the unit cell parameters of the xenotime solid solution follow Vegard's law, suggesting a random distribution of Er and Yb over the cation site in the xenotime structure. This further enables a complete thermodynamic analysis using a regular solution model, where the entropy of mixing is the dominating factor that controls the thermodynamic stability of $ErPO_4$-$YbPO_4$. It is expected that the use of a HREE solid solution or high-entropy xenotime ceramics as an environmental barrier coating or thermal barrier coating will be greatly benefited by the entropy-driven phase stabilization.

■ ASSOCIATED CONTENT

Supporting Information

The Supporting Information is available free of charge at https://pubs.acs.org/doi/10.1021/acsearthspacechem.2c00052.

XRF, FTIR, Raman, SEM, XRD, thermochemical data, entropy values, and heat capacities (PDF)

■ AUTHOR INFORMATION

Corresponding Author

Xiaofeng Guo − *Department of Chemistry and Alexandra Navrotsky Institute for Experimental Thermodynamics, Washington State University, Pullman, Washington 99164, United States; Materials Science and Engineering, Washington State University, Pullman, Washington 99164, United States;* orcid.org/0000-0003-3129-493X; Email: x.guo@wsu.edu

Authors

Andrew C. Strzelecki − *Department of Chemistry and Alexandra Navrotsky Institute for Experimental Thermodynamics, Washington State University, Pullman, Washington 99164, United States; Materials Science and Engineering, Washington State University, Pullman, Washington 99164, United States; Earth and Environmental Sciences Division, Los Alamos National Laboratory, Los Alamos, New Mexico 87545, United States*

Margaret Reece − *Department of Chemistry and Alexandra Navrotsky Institute for Experimental Thermodynamics, Washington State University, Pullman, Washington 99164, United States*

Xiaodong Zhao − *Department of Chemistry and Alexandra Navrotsky Institute for Experimental Thermodynamics, Washington State University, Pullman, Washington 99164, United States*

Wendy Yu − *Department of Chemistry and Alexandra Navrotsky Institute for Experimental Thermodynamics, Washington State University, Pullman, Washington 99164, United States;* Present Address: Department of Chemical Engineering, University of Michigan, Ann Arbor, Michigan 48109, United States

Chris Benmore − *X-ray Science Division, Argonne National Laboratory, Argonne, Illinois 60439, United States;* orcid.org/0000-0001-7007-7749

Yang Ren − *X-ray Science Division, Argonne National Laboratory, Argonne, Illinois 60439, United States; Department of Physics, City University of Hong Kong, Kowloon, Hong Kong 999077, China;* orcid.org/0000-0001-9831-6035

Christopher Alcorn − *Earth and Environmental Sciences Division, Los Alamos National Laboratory, Los Alamos, New Mexico 87545, United States*

Artaches Migdisov − *Earth and Environmental Sciences Division, Los Alamos National Laboratory, Los Alamos, New Mexico 87545, United States*

Hongwu Xu − *Earth and Environmental Sciences Division, Los Alamos National Laboratory, Los Alamos, New Mexico 87545, United States; School of Molecular Sciences, Center for Materials of the Universe, Arizona State University, Tempe, Arizona 85287, United States*

Complete contact information is available at: https://pubs.acs.org/10.1021/acsearthspacechem.2c00052

Notes

The authors declare no competing financial interest.

■ ACKNOWLEDGMENTS

We acknowledge the support by the institutional funds from the Department of Chemistry and New Faculty Seed Grant from ORAP at Washington State University in the early stage and the later support by the National Science Foundation (NSF), Division of Earth Sciences, under award no. 2149848. The research presented in this article was also supported by the Laboratory Directed Research and Development (LDRD) program of Los Alamos National Laboratory (LANL) under project 20180007DR. LANL, an affirmative action/equal opportunity employer, is managed by Triad National Security, LLC, for the National Nuclear Security Administration of the U.S. Department of Energy under contract 89233218CNA000001. Portions of this research were also supported by collaboration, services, and infrastructure through the Nuclear Science Center User Facility at WSU and the Alexandra Navrotsky Institute for Experimental Thermodynamics. Portions of this research used Beamline 6-ID-D (XSD-MM) and 11-ID-C (XSD-SRS) of the Advance Photon Source (APS), a U.S. DOE Office of Science User Facility operated for the DOE Office of Science by Argonne National Laboratory (ANL) under Contract DE-AC02-06CH11357. Lastly, we thank Dr. Rodney C. Ewing and Dr. Gorakh M. Pawar for discussion of this work.

■ REFERENCES

(1) Connelly, N. G.; Damhus, T.; Hartshorn, R. M.; Hutton, A. T. *Nomenclature of Inorganic Chemistry IUPAC Recommendations 2005 IUPAC Periodic Table of the Elements Fm No. (2005)*; 2005.

(2) Haxel, G. B.; Hedrick, J. B.; Orris, G. J. Rare Earth Elements—Critical Resources for High Technology. *United States Geological Survey Fact Sheet* 2002, *087*, 4, DOI: 10.1017/CBO9781107415324.004.

(3) Bunzli, J.-C. G.; McGill, I. Rare Earth Elements. In *Ullmann's Encyclopedia of Industrial Chemistry*; 2018.

(4) Han, J.; Wang, Y.; Liu, R.; Wan, F. Theoretical and Experimental Investigation of Xenotime-Type Rare Earth Phosphate $REPO_4$, (RE = Lu, Yb, Er, Y and Sc) for Potential Environmental Barrier Coating Applications. *Sci. Rep.* **2020**, *10*, 1−3.
(5) Herweyer, L. A.; Opila, E. J. High-Temperature Na_2SO_4 Interaction with Air Plasma Sprayed $Yb_2Si_2O_7$ + Si EBC System: Topcoat Behavior. *J. Am. Ceram. Soc.* **2021**, *104*, 6496−6507.
(6) Ridley, M.; Gaskins, J.; Hopkins, P.; Opila, E. J. Tailoring Thermal Properties of Multi-Component Rare Earth Monosilicates. *Acta Mater.* **2020**, *195*, 698−707.
(7) Golden, R. A.; Mueller, K.; Opila, E. J. Thermochemical Stability of $Y_2Si_2O_7$ in High-Temperature Water Vapor. *J. Am. Ceram. Soc.* **2020**, *103*, 4517−4535.
(8) Costa, G.; Harder, B. J.; Wiesner, V. L.; Jacobson, N. S.; Zhu, D.; Kapush, D.; Bansal, N.; Lee, K. N.; Ushakov, S. V.; Navrotsky, A. Thermodynamics of Reaction between Gas - Turbine Ceramic Coatings and Ingested CMAS Corrodents. *J. Am. Ceram. Soc.* **2019**, *102*, 2948−2964.
(9) Costa, G.; Harder, B. J.; Bansal, N. P.; Kowalski, B. A.; Stokes, J. L. Thermochemistry of Calcium Rare-Earth Silicate Oxyapatites. *J. Am. Ceram. Soc.* **2020**, *103*, 1446−1453.
(10) Ayyasamy, M. V.; Deijkers, J. A.; Wadley, H. N. G.; Balachandran, P. V. Density Functional Theory and Machine Learning Guided Search for $RE_2Si_2O_7$ with Targeted Coefficient of Thermal Expansion. *J. Am. Ceram. Soc.* **2020**, *103*, 4489−4497.
(11) Lee, K. N.; Fox, D. S.; Bansal, N. P. Rare Earth Silicate Environmental Barrier Coatings for SiC/SiC Composites and Si_3N_4 Ceramics. *J. Eur. Ceram. Soc.* **2005**, *25*, 1705−1715.
(12) Xu, Y.; Hu, X.; Xu, F.; Li, K. Rare Earth Silicate Environmental Barrier Coatings: Present Status and Prospective. *Ceram. Int.* **2017**, *43*, 5847−5855.
(13) Castor, S. B.; Hendrick, J. B. Rare Earth Elements. *Ind. Miner. Rocks* **2006**, 769−792.
(14) Dai, S.; Graham, I. T.; Ward, C. R. A Review of Anomalous Rare Earth Elements and Yttrium in Coal. *Int. J. Coal Geol.* **2016**, *159*, 82−95.
(15) Shannon, R. D. Revised Effective Ionic Radii and Systematic Studies of Interatomic Distances in Halides and Chalcogenides. *Acta Crystallogr., Sect. A: Cryst. Phys., Diffr., Theor. Gen. Crystallogr.* **1976**, *32*, 751−767.
(16) Kanazawa, Y.; Kamitani, M. Rare Earth Minerals and Resources in the World. *J. Alloys Compd.* **2006**, *408−412*, 1339−1343.
(17) Taggart, R. K.; Hower, J. C.; Dwyer, G. S.; Hsu-Kim, H. Trends in the Rare Earth Element Content of U. S.-Based Coal Combustion Fly Ashes. *Environ. Sci. Technol.* **2016**, *50*, 5919−5926.
(18) Williams-Jones, A. E.; Wollenberg, R.; Bodeving, S. Hydrothermal Fractionation of the Rare Earth Elements and the Genesis of the Lofdal REE Deposit, Namibia. In *Symposium on critical and strategic materials.* British Columbia Geological Survey Paper, 2015; pp. 125−130.
(19) Richter, L.; Diamond, L. W.; Atanasova, P.; Banks, D. A.; Gutzmer, J. Hydrothermal Formation of Heavy Rare Earth Element (HREE)- Xenotime Deposits at 100 °C in a Sedimentary Basin. *Geology* **2018**, *46*, 263−266.
(20) Li, M. Y. H.; Zhou, M. F.; Williams-Jones, A. E. The Genesis of Regolith-Hosted Heavy Rare Earth Element Deposits: Insights from the World-Class Zudong Deposit in Jiangxi Province, South China. *Econ. Geol.* **2019**, *114*, 541−568.
(21) Cook, N. J.; Ciobanu, C. L.; O'Rielly, D.; Wilson, R.; Das, K.; Wade, B. Mineral Chemistry of Rare Earth Element (REE) Mineralization, Browns Ranges, Western Australia. *Lithos* **2013**, *172-173*, 192−213.
(22) Gysi, A. P.; Harlov, D. Hydrothermal Solubility of $TbPO_4$, $HoPO_4$, $TmPO_4$, and $LuPO_4$ Xenotime Endmembers at PH of 2 and Temperatures between 100 and 250 °C. *Chem. Geol.* **2021**, *567*, 120072.
(23) Navrotsky, A.; Lee, W.; Mielewczyk-Gryn, A.; Ushakov, S. V.; Anderko, A.; Wu, H.; Riman, R. E. Thermodynamics of Solid Phases Containing Rare Earth Oxides. *J. Chem. Thermodyn.* **2015**, *88*, 126−141.
(24) Gysi, A. P.; Harlov, D.; Filho, D. C.; Williams-Jones, A. E. Experimental Determination of the High Temperature Heat Capacity of a Natural Xenotime-(Y) Solid Solution and Synthetic $DyPO_4$ and $ErPO_4$ Endmembers. *Thermochim. Acta* **2016**, *627-629*, 61−67.
(25) Ushakov, S. V.; Helean, K. B.; Navrotsky, A.; Boatner, L. A. Thermochemistry of Rare-Earth Orthophosphates. *J. Mater. Res.* **2001**, *16*, 2623−2633.
(26) Gysi, A. P.; Williams-Jones, A. E.; Harlov, D. The Solubility of Xenotime-(Y) and Other HREE Phosphates ($DyPO_4$, $ErPO_4$ and $YbPO_4$) in Aqueous Solutions from 100 to 250°C and Psat. *Chem. Geol.* **2015**, *401*, 83−95.
(27) Lacomba-Perales, R.; Errandonea, D.; Meng, Y.; Bettinelli, M. High-Pressure Stability and Compressibility of APO_4 (A=La, Nd, Eu, Gd, Er, and Y) Orthophosphates: An X-ray Diffraction Study Using Synchrotron Radiation. *Phys. Rev. B: Condens. Matter Mater. Phys.* **2010**, *81*, 1−9.
(28) Zhang, F. X.; Lang, M.; Ewing, R. C.; Lian, J.; Wang, Z. W.; Hu, J.; Boatner, L. A. Pressure-Induced Zircon-Type to Scheelite-Type Phase Transitions in $YbPO_4$ and $LuPO_4$. *J. Solid State Chem.* **2008**, *181*, 2633−2638.
(29) Gomis, O.; Lavina, B.; Rodríguez-Hernández, P.; Muñoz, A.; Errandonea, R.; Errandonea, D.; Bettinelli, M. High-Pressure Structural, Elastic, and Thermodynamic Properties of Zircon-Type $HoPO_4$ and $TmPO_4$. *J. Phys.: Condens. Matter* **2017**, *29*, No. 095401.
(30) López-Solano, J.; Rodríguez-Hernández, P.; Muñoz, A.; Gomis, O.; Santamaría-Perez, D.; Errandonea, D.; Manjón, F. J.; Kumar, R. S.; Stavrou, E.; Raptis, C. Theoretical and Experimental Study of the Structural Stability of $TbPO_4$ at High Pressures. *Phys. Rev. B: Condens. Matter Mater. Phys.* **2010**, *81*, 1−9.
(31) Migdisov, A.; Guo, X.; Nisbet, H.; Xu, H.; Williams-Jones, A. E. Fractionation of REE, U, and Th in Natural Ore-Forming Hydrothermal Systems: Thermodynamic Modeling. *J. Chem. Thermodyn.* **2019**, *128*, 305−319.
(32) Anderson, G. M.; Crerar, D. A. *Thermodynamics in Geochemistry: The Equilibrium Model*; Oxford University Press: New York, 1993.
(33) Konings, R. J. M.; Walter, M.; Popa, K. Excess Properties of the $(Ln_{2-2x}Ca_xTh_x)(PO_4)_2$ (Ln = La, Ce) Solid Solutions. *J. Chem. Thermodyn.* **2008**, *40*, 1305−1308.
(34) Popa, K.; Konings, R. J. M.; Geisler, T. High-Temperature Calorimetry of $(La_{1-x}Ln_x)PO_4$ Solid Solutions. *J. Chem. Thermodyn.* **2007**, *39*, 236−239.
(35) Popa, K.; Sedmidubský, D.; Beneš, O.; Thiriet, C.; Konings, R. J. M. The High-Temperature Heat Capacity of $LnPO_4$ (Ln = La, Ce, Gd) by Drop Calorimetry. *J. Chem. Thermodyn.* **2006**, *38*, 825−829.
(36) Ji, Y.; Kowalski, P. M.; Kegler, P.; Huittinen, N.; Marks, N. A.; Vinograd, V. L.; Arinicheva, Y.; Neumeier, S.; Bosbach, D. Rare-Earth Orthophosphates From Atomistic Simulations. *Front. Chem.* **2019**, *7*, 1−12.
(37) Mogilevsky, P. On the Miscibility Gap in Monazite-Xenotime Systems. *Phys. Chem. Miner.* **2007**, *34*, 201−214.
(38) Ridley, M.; McFarland, B.; Miller, C.; Opila, E. $YbPO_4$: A Novel Environmental Barrier Coating Candidate with Superior Thermochemical Stability. *Materialia* **2022**, *21*, 101289.
(39) Hikichi, Y.; Nomura, T. Melting Temperatures of Monazite and Xenotime. *J. Am. Ceram. Soc.* **1987**, *70*, C-252−C-253.
(40) Gavrichev, K. S.; Smirnova, N. N.; Gurevich, V. M.; Danilov, V. P.; Tyurin, A. V.; Ryumin, M. A.; Komissarova, L. N. Heat Capacity and Thermodynamic Functions of $LuPO_4$ in the Range 0-320 K. *Thermochim. Acta* **2006**, *448*, 63−65.
(41) Tyurin, A. V.; Ryumin, M. A.; Khoroshilov, A. V.; Gurevich, V. M.; Gavrichev, K. S. Thermodynamic Functions of Holmium Orthophosphate $HoPO_4$ in the Range 9−1370 K. *Thermochim. Acta* **2020**, *683*, 178459.
(42) Gavrichev, K. S.; Ryumin, M. A.; Tyurin, A. V.; Gurevich, V. M.; Nikiforova, G. E.; Komissarova, L. N. Heat Capacity and

https://doi.org/10.1021/acsearthspacechem.2c00052
ACS Earth Space Chem. 2022, 6, 1375−1389

Thermodynamic Functions of $YbPO_4$ from 0 to 1800 K. *Inorg. Mater.* **2013**, *49*, 701−708.
(43) Gavrichev, K. S.; Ryumin, M. A.; Tyurin, A. V.; Gurevich, V. M.; Khoroshilov, A. V.; Komissarova, L. N. Thermodynamic Functions of Erbium Orthophosphate $ErPO_4$ in the Temperature Range of 0-1600 K. *Thermochim. Acta* **2012**, *535*, 1−7.
(44) Gavrichev, K. S.; Ryumin, M. A.; Tyurin, A. V.; Gurevich, V. M.; Komissarova, L. N. Heat Capacity and Thermodynamic Functions of Xenotime YPO_4(c) at 0-1600 K. *Geochem. Int.* **2010**, *48*, 932−939.
(45) Goncharov, V. G.; Nisbet, H.; Strzelecki, A.; Benmore, C. J.; Migdisov, A. A.; Xu, H.; Guo, X. Energetics of Hydroxylbastnäsite Solid Solutions, $La_{1-x}Nd_xCO_3OH$. *Geochim. Cosmochim. Acta* **2022**, DOI: 10.1016/j.gca.2022.04.002.
(46) Ewing, R. C.; Wang, L. M. Phosphates as Nuclear Waste Forms. In *Phosphates: Geochemical, Geobiological and Materials Importance*; Kohn, M. J., Rakovan, J., Hughes, J. M., Eds.; Mineralogical Society of America, 2002; Vol. *48*, pp. 673−700, DOI: 10.2138/rmg.2002.48.18.
(47) Boatner, L. A. Synthesis, Structure, and Properties of Monazite, Pretulite, and Xenotime. *Rev. Mineral. Geochem.* **2002**, *48*, 87−121.
(48) Orlova, A. I.; Ojovan, M. I. Ceramic Mineral Waste-Forms for Nuclear Waste Immobilization. *Materials* **2019**, *12*, 2638.
(49) Rafiuddin, M. R.; Grosvenor, A. P. Probing the Effect of Radiation Damage on the Structure of Rare-Earth Phosphates. *J. Alloys Compd.* **2015**, *653*, 279−289.
(50) Boatner, L. A.; Abraham, M. M.; Sales, B. C. Lanthanide Orthophosphate Ceramics for the Disposal of Actinide-Contaminated Nuclear Wastes. *Inorg. Chim. Acta* **1984**, *94*, 146−148.
(51) Lumpkin, G. R. Ceramic Waste Forms for Actinides. *Elements* **2006**, *2*, 365−372.
(52) Vance, E. R.; Zhang, Y.; McLeod, T.; Davis, J. Actinide Valences in Xenotime and Monazite. *J. Nucl. Mater.* **2011**, *409*, 221−224.
(53) Cotton, S. *Lanthanide and Actinide Chemistry*; John Wiley & Sons, Ltd., 2006.
(54) Morss, L. R.; Edelstein, N. M.; Fuger, J. *The Chemistry of the Actinides and Transactinide Elements, Fourth*; Morss, L. R., Edelstein, N. M., Fuger, J., Eds.; Springer: Dordrecht, 2010.
(55) Strzelecki, A. C.; Bourgeois, C.; Kriegsman, K. W.; Estevenon, P.; Wei, N.; Szenknect, S.; Mesbah, A.; Wu, D.; Ewing, R. C.; Dacheux, N.; Guo, X. Thermodynamics of $CeSiO_4$: Implications for Actinide Orthosilicates. *Inorg. Chem.* **2020**, *59*, 13174−13183.
(56) Guo, X.; Szenknect, S.; Mesbah, A.; Labs, S.; Clavier, N.; Poinssot, C.; Ushakov, S. V.; Curtius, H.; Bosbach, D.; Ewing, R. C.; Burns, P. C.; Dacheux, N.; Navrotsky, A. Thermodynamics of Formation of Coffinite, $USiO_4$. *Proc. Natl. Acad. Sci.* **2015**, *112*, 6551−6555.
(57) Guo, X.; Szenknect, S.; Mesbah, A.; Clavier, N.; Poinssot, C.; Wu, D.; Xu, H.; Dacheux, N.; Ewing, R. C.; Navrotsky, A. Energetics of a Uranothorite ($Th_{1-x}U_xSiO_4$) Solid Solution. *Chem. Mater.* **2016**, *28*, 7117−7124.
(58) Hobart, D. E.; Begun, G. M.; Haire, R. G.; Hellwege, H. E. Raman Spectra of the Transplutonium Orthophosphates and Trimetaphosphates. *J. Raman Spectrosc.* **1983**, *14*, 59−62.
(59) Popa, K.; Vigier, J. F.; Martel, L.; Manara, D.; Colle, J. Y.; Blanco, O. D.; Wiss, T.; Freis, D.; Konings, R. J. M. Synthesis, Characterization, and Stability of Americium Phosphate, $AmPO_4$. *Inorg. Chem.* **2020**, *59*, 6595−6602.
(60) Bjorklund, C. W. The Preparation of PuP_2O_7 and $PuPO_4$. *J. Am. Chem. Soc.* **1957**, *19*, 6347−6350.
(61) Begg, B. D.; Vance, E. R.; Conradson, S. D. The Incorporation of Plutonium and Neptunium in Zirconolite and Perovskite. *J. Alloys Compd.* **1998**, *271-273*, 221−226.
(62) Szenknect, S.; Costin, D. T.; Clavier, N.; Mesbah, A.; Poinssot, C.; Vitorge, P.; Dacheux, N. From Uranothorites to Coffinite: A Solid Solution Route to the Thermodynamic Properties of $USiO_4$. *Inorg. Chem.* **2013**, *52*, 6957−6968.
(63) Marcial, J.; Zhang, Y.; Zhao, X.; Xu, H.; Mesbah, A.; Nienhuis, E. T.; Szenknect, S.; Neuefeind, J. C.; Lin, J.; Qi, L.; Migdisov, A. A.; Ewing, R. C.; Dacheux, N.; McCloy, J. S.; Guo, X. Thermodynamic Non-Ideality and Disorder Heterogeneity in Actinide Silicate Solid Solutions. *npj Mater. Degrad.* **2021**, *5*, 1−14.
(64) Mesbah, A.; Clavier, N.; Lozano-Rodriguez, M. J.; Szenknect, S.; Dacheux, N. Incorporation of Thorium in the Zircon Structure Type through the $Th_{1-x}Er_x(SiO4)_{1-x}(PO_4)_x$ Thorite-Xenotime Solid Solution. *Inorg. Chem.* **2016**, *55*, 11273−11282.
(65) Bruker Nano GmbH. *S2 Picofox*; Bruker Nano GmbH: Berlin 2010.
(66) Bruker Nano GmbH. *Spectra 7*. Bruker Nano GmbH: Berlin 2010.
(67) Strzelecki, A. C.; Kriegsman, K.; Estevenon, P.; Goncharov, V.; Bai, J.; Szenknect, S.; Mesbah, A.; Wu, D.; McCloy, J. S.; Dacheux, N.; Guo, X. High-Temperature Thermodynamics of Cerium Silicates, A-$Ce_2Si_2O_7$ and $Ce_{4.67}(SiO_4)_3O$. *ACS Earth Space Chem.* **2020**, *4*, 2129−2143.
(68) Nienhuis, E. T.; Saleh, M.; Marcial, J.; Kriegsman, K.; Lonergan, J.; Lipton, A. S.; Guo, X.; McCloy, J. S. Structural Characterization of $ZnSO_4$-K_2SO_4-NaCl Glasses. *J. Non-Cryst. Solids* **2019**, *524*, 119639.
(69) Olds, T. A.; Karcher, S. E.; Kriegsman, K. W.; Guo, X.; McCloy, J. S. Oxidation and Anion Lattice Defect Signatures of Hypostoichiometric Lanthanide-Doped UO_2. *J. Nucl. Mater.* **2020**, *530*, 151959.
(70) Lenz, C.; Nasdala, L.; Talla, D.; Hauzenberger, C.; Seitz, R.; Kolitsch, U. Laser-Induced REE3+ Photoluminescence of Selected Accessory Minerals - An "Advantageous Artefact" in Raman Spectroscopy. *Chem. Geol.* **2015**, *415*, 1−16.
(71) Prescher, C.; Prakapenka, V. B. DIOPTAS: A Program for Reduction of Two-Dimensional X-Ray Diffraction Data and Data Exploration. *High Pressure Res.* **2015**, *35*, 223−230.
(72) Toby, B. H.; Von Dreele, R. B. GSAS-II: The Genesis of a Modern Open-Source All Purpose Crystallography Software Package. *J. Appl. Crystallogr.* **2013**, *46*, 544−549.
(73) Strzelecki, A. C.; Ren, Y.; Chong, S.; Riley, B. J.; Xu, H.; McCloy, J. S.; Guo, X. Structure and Thermodynamics of Calcium Rare Earth Silicate Oxyapatites, $Ca_2RE_8(SiO_4)_6O_2$ (RE = Pr, Tb, Ho, Tm). *Phys. Chem. Miner.* **2022**, DOI: 10.1007/s00269-022-01187-5.
(74) Strzelecki, A. C.; Barral, T.; Estevenon, P.; Mesbah, A.; Goncharov, V.; Baker, J.; Bai, J.; Clavier, N.; Szenknect, S.; Migdisov, A.; Xu, H.; Ewing, R. C.; Dacheux, N.; Guo, X. The Role of Water and Hydroxyl Groups in the Structures of Stetindite and Coffinite, $MSiO_4$ (M = Ce, U). *Inorg. Chem.* **2021**, *60*, 718−735.
(75) Xu, H.; Chavez, M. E.; Mitchell, J. N.; Garino, T. J.; Schwarz, H. L.; Rodriguez, M. A.; Rademacher, D. X.; Nenoff, T. M. Crystal Structure and Thermodynamic Stability of Ba/Ti-Substituted Pollucites for Radioactive Cs/Ba Immobilization. *J. Am. Ceram. Soc.* **2015**, *98*, 2634−2640.
(76) Xu, H.; Guo, X.; Bai, J. Thermal Behavior of Polyhalite: A High-Temperature Synchrotron XRD Study. *Phys. Chem. Miner.* **2017**, *44*, 125−135.
(77) Guo, X.; Lü, X.; White, J. T.; Benmore, C. J.; Nelson, A. T.; Roback, R. C.; Xu, H. Bulk Moduli and High Pressure Crystal Structure of U_3Si_2. *J. Nucl. Mater.* **2019**, *523*, 135−142.
(78) Tavakoli, A. H.; Maram, P. S.; Widgeon, S. J.; Rufner, J.; Van Benthem, K.; Ushakov, S.; Sen, S.; Navrotsky, A. Amorphous Alumina Nanoparticles: Structure, Surface Energy, and Thermodynamic Phase Stability. *J. Phys. Chem. C* **2013**, *117*, 17123−17130.
(79) Guo, X.; Tiferet, E.; Qi, L.; Solomon, J. M.; Lanzirotti, A.; Newville, M.; Engelhard, M. H.; Kukkadapu, R. K.; Wu, D.; Ilton, E. S.; Asta, M.; Sutton, S. R.; Xu, H.; Navrotsky, A. U(v) in Metal Uranates: A Combined Experimental and Theoretical Study of $MgUO_4$, $CrUO_4$, and $FeUO_4$. *Dalton Trans.* **2016**, *45*, 4622−4632.
(80) Guo, X.; Wu, D.; Xu, H.; Burns, P. C.; Navrotsky, A. Thermodynamic Studies of Studtite Thermal Decomposition Pathways via Amorphous Intermediates UO_3, U_2O_7, and UO_4. *J. Nucl. Mater.* **2016**, *478*, 158−163.

(81) Navrotsky, A. Progress and New Directions in Calorimetry: A 2014 Perspective. *J. Am. Ceram. Soc.* **2014**, *97*, 3349−3359.
(82) Zhang, X.; Reece, M. E.; Cockreham, C. B.; Sun, H.; Wang, B.; Xu, H.; Sun, J.; Guo, X.; Su, H.; Wang, Y.; Wu, D. Formation Energetics and Guest—Host Interactions of Molybdenum Carbide Confined in Zeolite Y. *Ind. Eng. Chem. Res.* **2021**, 13991.
(83) Ni, Y.; Hughes, J. M.; Mariano, A. N. Crystal Chemistry of the Monazite and Xenotime Structures. *Am. Mineral.* **1995**, *80*, 21−26.
(84) Estevenon, P.; Welcomme, E.; Szenknect, S.; Mesbah, A.; Moisy, P.; Poinssot, C.; Dacheux, N. Preparation of $CeSiO_4$ from Aqueous Precursors under Soft Hydrothermal Conditions. *Dalton Trans.* **2019**, *48*, 7551−7559.
(85) Estevenon, P.; Kaczmarek, T.; Vadot, F.; Dumas, T.; Solari, P. L.; Welcomme, E.; Szenknect, S.; Mesbah, A.; Moisy, P.; Poinssot, C.; Dacheux, N. Formation of $CeSiO_4$ from Cerium (III) Silicate Precursors. *Dalton Trans.* **2019**, *48*, 10455−10463.
(86) Estevenon, P.; Kaczmarek, T.; Rafiuddin, M. R.; Welcomme, E.; Szenknect, S.; Mesbah, A.; Moisy, P.; Poinssot, C.; Dacheux, N. Soft Hydrothermal Synthesis of Hafnon, $HfSiO_4$. *Cryst. Growth Des.* **2020**, *20*, 1820−1828.
(87) Estevenon, P.; Welcomme, E.; Tamain, C.; Jouan, G.; Szenknect, S.; Mesbah, A.; Poinssot, C.; Moisy, P.; Dacheux, N. The Formation of $PuSiO_4$ under Hydrothermal Conditions. *Dalton Trans.* **2020**, *49*, 6434−6445.
(88) Estevenon, P.; Welcomme, E.; Szenknect, S.; Mesbah, A.; Moisy, P.; Poinssot, C.; Dacheux, N. Multiparametric Study of the Synthesis of $ThSiO_4$ under Hydrothermal Conditions. *Inorg. Chem.* **2018**, *57*, 9393−9402.
(89) Estevenon, P.; Dumas, T.; Solari, P. L.; Welcomme, E.; Szenknect, S.; Mesbah, A.; Kvashnina, K. O.; Moisy, P.; Poinssot, C.; Dacheux, N. Formation of Plutonium(IV) Silicate Species in Very Alkaline Reactive Media. *Dalton Trans.* **2021**, *50*, 12528−12536.
(90) Pavlik, A., III; Ushakov, S. V.; Navrotsky, A.; Benmore, C. J.; Weber, R. J. K. Structure and Thermal Expansion of Lu_2O_3 and Yb_2O_3 up to the Melting Points. *J. Nucl. Mater.* **2017**, *495*, 385−391.
(91) Clavier, N.; Szenknect, S.; Costin, D. T.; Mesbah, A.; Ravaux, J.; Poinssot, C.; Dacheux, N. Purification of Uranothorite Solid Solutions from Polyphase Systems. *J. Nucl. Mater.* **2013**, *441*, 73−83.
(92) Nasdala, L.; Zhang, M.; Kempe, U.; Panczer, G.; Gaft, M.; Andrut, M.; Plötze, M. Spectroscopic Methods Applied to Zircon. *Rev. Mineral. Geochem.* 2003, 427−467, DOI: 10.2113/0530427.
(93) Dawson, P.; Hargreave, M. M.; Wilkinson, G. R. The Vibrational Spectrum of Zircon ($ZrSiO_4$). *J. Phys. C: Solid State Phys.* **1971**, *4*, 240−256.
(94) Clavier, N.; Szenknect, S.; Costin, D. T.; Mesbah, A.; Poinssot, C.; Dacheux, N. From Thorite to Coffinite: A Spectroscopic Study of $Th_{1-x}U_xSiO_4$ Solid Solutions. *Spectrochim. Acta, Part A* **2014**, *118*, 302−307.
(95) Clavier, N.; Mesbah, A.; Szenknect, S.; Dacheux, N. Monazite, Rhabdophane, Xenotime & Churchite: Vibrational Spectroscopy of Gadolinium Phosphate Polymorphs. *Spectrochim. Acta, Part A* **2018**, *205*, 85−94.
(96) Nasdala, L.; Beran, A.; Libowitzky, E.; Wolf, D. The Incorporation of Hydroxyl Groups and Molecular Water in Natural Zircon ($ZrSiO_4$). *Am. J. Sci.* **2001**, *301*, 831−857.
(97) Abe, T.; Kuribayashi, T.; Nakamura, M. OH Defects in Synthetic Xenotime (YPO_4). *Eur. J. Mineral.* **2016**, *28*, 641−648.
(98) Talla, D.; Beran, A.; Škoda, R.; Losos, Z. On the Presence of OH Defects in the Zircon-Type Phosphate Mineral Xenotime, $(Y,REE)PO_4$. *Am. Mineral.* **2011**, *96*, 1799−1808.
(99) Kolesov, B. A.; Geiger, C. A.; Armbruster, T. The Dynamic Properties of Zircon Studied by Single-Crystal X-ray Diffraction and Raman Spectroscopy. *Eur. J. Mineral.* **2001**, *13*, 939−948.
(100) Hoskin, P. W. O.; Rodgers, K. A. Raman Spectral Shift in the Isomorphous Series $(Zr_{1-x}Hf_x)$ SiO_4. *Eur. J. Solid State Inorg. Chem.* **1996**, *33*, 1111−1121.
(101) Syme, R. W. G.; Lockwood, D. J.; Kerr, H. J. Raman Spectrum of Synthetic Zircon ($ZrSiO_4$) and Thorite ($THSiO_4$). *J. Phys. C: Solid State Phys.* **1977**, *10*, 1335−1348.
(102) Begun, G. M.; Beall, G. W.; Boatner, L. A.; Gregor, W. J. Raman Spectra of the Rare Earth Orthophosphates. *J. Raman Spectrosc.* **1982**, *11*, 273−278.
(103) Caruba, R.; Baumer, A.; Ganteaume, M.; Iacconi, P. An Experimental Study of Hydroxyl Groups and Water in Synthetic and Natural Zircons: A Model of the Metamict State. *Am. Mineral.* **1985**, *70*, 1224−1231.
(104) Janeczek, J. Composition and Origin of Coffinite from Jachymov. Czechoslovakia. *Neues Jahrb. Mineral., Monatsh.* **1991**, *9*, 385−395.
(105) Kijkowska, R. Thermal Decomposition of Lanthanide Orthophosphates Synthesized through Crystallisation from Phosphoric Acid Solution. *Thermochim. Acta* **2003**, *404*, 81−88.
(106) Nasdala, L.; Schmidt, C. Applications of Raman Spectroscopy in Mineralogy and Geochemistry. *Elements* **2020**, *16*, 99−104.
(107) Pasteris, J. D.; Beyssac, O. Welcome to Raman Spectroscopy: Successes, Challenges, and Pitfalls. *Elements* **2020**, *16*, 87−92.
(108) Chen, Y.; Zou, C.; Mastalerz, M.; Hu, S.; Gasaway, C.; Tao, X. Applications of Micro-Fourier Transform Infrared Spectroscopy (FTIR) in the Geological Sciences—A Review. *Int. J. Mol. Sci.* **2015**, *16*, 30223−30250.
(109) Zhukova, I. A.; Stepanov, A. S.; Korsakov, A. V.; Jiang, S.-Y. Application of Raman Spectroscopy for the Identification of Phosphate Minerals from REE Supergene Deposit. *J. Raman Spectrosc.* **2022**, 485−496.
(110) Föster, H.-J. The Chemical Composition of REE-Y-Th-U-Rich Accessory Minerals in Peraluminous Granites of the Erzgebirge-Fichtelgebirge Region, Germany, Part I: The Monazite- (Ce) -Brabantite Solid Solution Series. *Am. Mineral.* **1998**, *83*, 259−272.
(111) Nesse, W. D. *Introduction to Mineralogy*; 2nd ed.; Oxford University Press, 2000.
(112) Onac, B. P.; Ettinger, K.; Kearns, J.; Balasz, I. I. A Modern, Guano-Related Occurrence of Foggite, $CaAl(PO_4)(OH)_2{\cdot}H_2O$ and Churchite-(Y), $YPO_4{\cdot}2H_2O$ in Cioclovina Cave, Romania. *Mineral. Petrol.* **2005**, *85*, 291−302.
(113) Frost, R. L.; Sejkora, J.; Keeffe, E. C.; Plášil, J.; Čejka, J.; Bahfenne, S. Raman Spectroscopic Study of the Phosphate Mineral Churchite-(Y), $YPO_4{\cdot}2H_2O$. *J. Raman Spectrosc.* **2010**, *41*, 202−206.
(114) Subramani, T.; Rafiuddin, M. R.; Shelyug, A.; Ushakov, S. V.; Mesbah, A.; Clavier, N.; Qin, D.; Szenknect, S.; Elkaim, E.; Dacheux, N.; Navrotsky, A. Synthesis, Crystal Structure and Enthalpies of Formation of Churchite-Type $REPO_4{\cdot}2H_2O$ (RE = Gd to Lu) Materials. *Cryst. Growth Des.* **2019**, *19*, 4641−4649.
(115) Taylor, S. R.; Mclennan, S. M. The Geochemical Evolution of the Continental Crust. *Am. Geophys. Union* **1995**, *33*, 241−265.
(116) Giarola, M.; Sanson, A.; Rahman, A.; Mariotto, G.; Bettinelli, M.; Speghini, A.; Cazzanelli, E. Vibrational Dynamics of YPO_4 and $ScPO_4$ Single Crystals: An Integrated Study by Polarized Raman Spectroscopy and First-Principles Calculations. *Phys. Rev. B: Condens. Matter Mater. Phys.* **2011**, *83*, 1−8.
(117) Maftei, A. E.; Buzatu, A.; Damian, G.; Buzgar, N.; Dill, H. G.; Apopei, A. I. Micro-Raman—A Tool for the Heavy Mineral Deposits, Gold Placer-Type (Pianu Valley, Romania). *Minerals* **2020**, *10*, 1−17.
(118) Švecová, E.; Čopjaková, R.; Losos, Z.; Škoda, R.; Nasdala, L.; Cícha, J. Multi-Stage Evolution of Xenotime−(Y) from Písek Pegmatites, Czech Republic: An Electron Probe Micro-Analysis and Raman Spectroscopy Study. *Mineral. Petrol.* **2016**, *110*, 747−765.
(119) Origlieri, M. *Xenotime-(Y) R050178*.
(120) Obodda, H. *Xenotime-(Y) R060428*.
(121) Moëlo, Y.; Lulzac, Y.; Rouer, O.; Palvadeau, P.; Gloaguen, É.; Léone, P. Scandium Mineralogy: Pretulite with Scandian Zircon and Xenotime-(Y) within an Apatite-Rich Oolitic Ironstone from Saint-Aubin-Des-Châteaux, Armorican Massif, France. *Can. Mineral.* **2002**, *40*, 1657−1673.
(122) Xu, H.; Navrotsky, A.; Su, Y.; Balmer, M. L. Perovskite Solid Solutions along the $NaNbO_3$-$SrTiO_3$ Join: Phase Transitions, Formation Enthalpies, and Implications for General Perovskite Energetics. *Chem. Mater.* **2005**, *17*, 1880−1886.

(123) Xu, H.; Su, Y.; Balmer, M. L.; Navrotsky, A. A New Series of Oxygen-Deficient Perovskites in the $NaTi_xNb_{1-x}O_{3-0.5x}$ System: Synthesis, Crystal Chemistry, and Energetics. *Chem. Mater.* **2003**, *15*, 1872−1878.
(124) Xu, H.; Navrotsky, A.; Balmer, M. L.; Su, Y.; Bitten, E. R. Energetics of Substituted Pollucites Along the $CsAlSi_2O_6$−$CsTiSi_2O_{6.5}$ Join : A High-Temperature Calorimetric Study. *J. Am. Ceram. Soc.* **2001**, *84*, 555−560.
(125) Xu, H.; Navrotsky, A.; Nyman, M. D.; Nenoff, T. M. Octahedral Microporous Phases Na_2Nb_{2-x} Ti_xO_{6-x} $(OH)_x{\cdot}H_2O$ and Their Related Perovskites: Crystal Chemistry, Energetics, and Stability Relations. *J. Mater. Res.* **2005**, *20*, 618−627.
(126) Hirsch, A.; Kegler, P.; Alencar, I.; Ruiz-Fuertes, J.; Shelyug, A.; Peters, L.; Schreinemachers, C.; Neumann, A.; Neumeier, S.; Liermann, H.-P.; Navrotsky, A.; Roth, G. Structural, Vibrational, and Thermochemical Properties of the Monazite-Type Solid Solution $La_{1-x}Pr_xPO_4$. *J. Solid State Chem.* **2017**, *245*, 82−88.
(127) Schlenz, H.; Dellen, J.; Kegler, P.; Gatzen, C.; Schreinemachers, C.; Shelyug, A.; Klinkenberg, M.; Navrotsky, A.; Bosbach, D. Structural and Thermodynamic Mixing Properties of $La_{1-x}Nd_xPO_4$ Monazite-Type Solid Solutions. *J. Solid State Chem.* **2019**, *270*, 470−478.
(128) Ganguly, J.; Cheng, W.; O'Neill, H. S. C. Syntheses, Volume, and Structural Changes of Garnets in the Pyrope-Grossular Join: Implications for Stability and Mixing Properties. *Am. Mineral.* **1993**, *78*, 583−593.
(129) Glynn, P. Solid-Solution Solubilities and Thermodynamics: Sulfates, Carbonates and Halides. *Rev. Mineral. Geochem.* **2000**, *40*, 481−511.
(130) Jenkins, H. D. B.; Glasser, L. Standard Absolute Entropy, S_{298}°, Values from Volume or Density. 1. Inorganic Materials. *Inorg. Chem.* **2003**, *42*, 8702−8708.
(131) Glasser, L. Thermodynamics of Condensed Phases: Formula Unit Volume, Vm, and the Determination of the Number of Formula Units, Z, in a Crystallographic Unit Cell. *J. Chem. Educ.* **2011**, *88*, 581−585.
(132) Guo, X.; Xu, H. Enthalpies of Formation of Polyhalite: A Mineral Relevant to Salt Repository. *J. Chem. Thermodyn.* **2017**, *114*, 44−47.
(133) Robie, R. A.; Hemingway, B. S. Thermodynamic Properties of Minerals and Related Substances at 298.15 K and 1 Bar (105 Pascal) Pressure and at Higher Temperatures. *U.S. Geol. Surv. Bull.* **1995**, 2131.
(134) Migdisov, A.; Williams-Jones, A. E.; Brugger, J.; Caporuscio, F. A. Hydrothermal Transport, Deposition, and Fractionation of the REE: Experimental Data and Thermodynamic Calculations. *Chem. Geol.* **2016**, *439*, 13−42.
(135) Van Hoozen, C. J.; Gysi, A. P.; Harlov, D. E. The Solubility of Monazite ($LaPO_4$, $PrPO_4$, $NdPO_4$, and $EuPO_4$) Endmembers in Aqueous Solutions from 100 to 250 °C. *Geochim. Cosmochim. Acta* **2020**, *280*, 302−316.
(136) Majzlan, J.; Zittlau, A. H.; Grevel, K.-D.; Schliesser, J.; Woodfield, B. F.; Dachs, E.; Števko, M.; Chovan, M.; Plášil, J.; Sejkora, J.; Milovská, S. Thermodynamic Properties and Phase Equilibria of the Secondary Copper Minerals Libethenite, Olivenite, Pseudomalachite, Kröhnkite, Cyanochroite, and Devilline. *Can. Mineral.* **2015**, *53*, 937−960.
(137) Vieillard, P.; Tardy, Y. Thermochemical Properties of Phosphates. *Phosphate Miner.* **1984**, 171−198.
(138) Nord, A. G.; Kierkegaard, P. The Crystal Structure of $Mg_3(PO_4)_2$. *Acta Chem. Scand.* **1968**, *22*, 1466−1474.
(139) Catti, M.; Ferraris, G.; Filhol, A. Hydrogen Bonding in the Crystalline State. CaHPO4 (Monetite), $P\bar{1}$ or P1? A Novel Neutron Diffraction Study. *Acta Crystallogr., Sect. B: Struct. Crystallogr. Cryst. Chem.* **1977**, *33*, 1223−1229.
(140) Schofield, P. F.; Knight, K. S.; van der Houwen, J. A. M.; Valsami-Jones, E. The Role of Hydrogen Bonding in the Thermal Expansion and Dehydration of Brushite, Di-Calcium Phosphate Dihydrate. *Phys. Chem. Miner.* **2004**, *31*, 606−624.
(141) Kniep, R.; Mootz, D.; Vegas, A. Variscite. *Acta Crystallogr., Sect. B: Struct. Crystallogr. Cryst. Chem.* **1977**, *33*, 263−265.
(142) Gorfman, S.; Tsirelson, V.; Pucher, A.; Morgenroth, W.; Pietsch, U. X-Ray Diffraction by a Crystal in a Permanent External Electric Field: Electric-Field-Induced Structural Response in α-$GaPO_4$. *Acta Crystallogr., Sect. A: Found. Crystallogr.* **2006**, *62*, 1−10.
(143) Angel, R. J.; Bismayer, U.; Marshall, W. G. Renormalization of the Phase Transition in Lead Phosphate, $Pb_3(PO_4)_2$, by High Pressure: Structure. *J. Phys.: Condens. Matter* **2001**, *13*, 5353−5364.
(144) Kampf, A. R. Minyulite; Its Atomic Arrangement. *Am. Mineral.* **1977**, *62*, 256−262.
(145) Moore, P. B.; Araki, T. Trolleite, $Al_4(OH)_3[PO_4]_3$: A Very Dense Structure with Octahedral Face-Sharing Dimers. *Am. Mineral.* **1974**, *59*, 974−984.
(146) Bulina, N. V.; Makarova, S. V.; Prosanov, I. Y.; Vinokurova, O. B.; Lyakhov, N. Z. Structure and Thermal Stability of Fluorhydroxyapatite and Fluorapatite Obtained by Mechanochemical Method. *J. Solid State Chem.* **2020**, *282*, 121076.
(147) Fang, Y. N.; Ritter, C.; White, T. J. Crystal Chemical Characteristics of Ellestadite-Type Apatite: Implications for Toxic Metal Immobilization. *Dalton Trans.* **2014**, *43*, 16031−16043.
(148) Drouet, C. A Comprehensive Guide to Experimental and Predicted Thermodynamic Properties of Phosphate Apatite Minerals in View of Applicative Purposes. *J. Chem. Thermodyn.* **2015**, *81*, 143−159.
(149) Hata, M.; Marumo, F.; Iwai, S.; Aoki, H. Structure of Barium Chlorapatite. *Acta Crystallogr., Sect. B: Struct. Crystallogr. Cryst. Chem.* **1979**, *35*, 2382−2384.
(150) Chen, J.; Liang, Y.; Zhu, Y.; Liu, S.; Li, H.; Lei, W. Abnormal Reduction of Eu^{3+} to Eu^{2+} in $Sr_5(PO_4)_3Cl$:Eu Phosphor and Its Enhanced Red Emission by the Charge Compensation. *J. Lumin.* **2019**, *214*, 116569.
(151) Elliott, J. C.; Dykes, E.; Mackie, P. E. Structure of Bromapatite and the Radius of the Bromide Ion. *Acta Crystallogr., Sect. B: Struct. Crystallogr. Cryst. Chem.* **1981**, *37*, 435−438.
(152) Suleimanov, E. V.; Chernorukov, N. G.; Veridusova, V. V.; Nipruk, O. V. Physical Chemistry of Barium Uranophosphate and Uranoarsenate. *Radiochemistry* **2006**, *48*, 155−158.
(153) Miller, S. A.; Taylor, J. C. The crystal structure of saleeite, $Mg[UO_2PO_4]_2{\cdot}10H_2O$. *Z. Kristallogr. - Cryst. Mater.* **1986**, *177*, 247−253.
(154) Lothenbach, B.; Xu, B.; Winnefeld, F. Thermodynamic Data for Magnesium (Potassium) Phosphates. *Appl. Geochem.* **2019**, *111*, 104450.
(155) Szenknect, S.; Mesbah, A.; Cordara, T.; Clavier, N.; Brau, H. P.; Le Goff, X.; Poinssot, C.; Ewing, R. C.; Dacheux, N. First Experimental Determination of the Solubility Constant of Coffinite. *Geochim. Cosmochim. Acta* **2016**, *181*, 36−53.
(156) Banks, D. A.; Yardley, B. W. D.; Campbell, A. R.; Jarvis, K. E. REE Composition of an Aqueous Magmatic Fluid: A Fluid Inclusion Study from the Capitan Pluton, New Mexico, USA. *Chem. Geol.* **1994**, *113*, 259−272.
(157) Smith, M. P.; Henderson, P.; Campbell, L. S. Fractionation of the REE during Hydrothermal Processes: Constraints from the Bayan Obo Fe-REE-Nb Deposit, Inner Mongolia, China. *Geochim. Cosmochim. Acta* **2000**, *64*, 3141−3160.
(158) Williams-Jones, A. E.; Samson, I. M.; Olivo, G. R. The Genesis of Hydrothermal Fluorite-REE Deposits in the Gallinas Mountains, New Mexico. *Econ. Geol.* **2000**, *95*, 327−341.
(159) Lehmann, B.; Nakai, S.; Höhndorf, A.; Brinckmann, J.; Dulski, P.; Hein, U. F.; Masuda, A. REE Mineralization at Gakara, Burundi: Evidence for Anomalous Upper Mantle in the Western Rift Valley. *Geochim. Cosmochim. Acta* **1994**, *58*, 985−992.
(160) Clavier, N.; Podor, R.; Dacheux, N. Crystal Chemistry of the Monazite Structure. *J. Eur. Ceram. Soc.* **2011**, *31*, 941−976.
(161) Migdisov, A. A.; Williams-Jones, A. E.; Wagner, T. An Experimental Study of the Solubility and Speciation of the Rare Earth Elements (III) in Fluoride- and Chloride-Bearing Aqueous Solutions

at Temperatures up to 300 °C. *Geochim. Cosmochim. Acta* **2009**, *73*, 7087−7109.
(162) Williams-Jones, A. E.; Migdisov, A. A.; Samson, I. M. Hydrothermal Mobilisation of the Rare Earth Elements-a Tale of "Ceria" and "Yttria.". *Elements* **2012**, *8*, 355−360.
(163) Mayanovic, R. A.; Jayanetti, S.; Anderson, A. J.; Bassett, W. A.; Chou, I. M. The Structure of Yb^{3+} Aquo Ion and Chloro Complexes in Aqueous Solutions at up to 500 °C and 270 MPa. *J. Phys. Chem. A* **2002**, *106*, 6591−6599.
(164) Mayanovic, R. A.; Anderson, A. J.; Bassett, W. A.; Chou, I. M. On the Formation and Structure of Rare-Earth Element Complexes in Aqueous Solutions under Hydrothermal Conditions with New Data on Gadolinium Aqua and Chloro Complexes. *Chem. Geol.* **2007**, *239*, 266−283.
(165) Mayanovic, R. A.; Anderson, A. J.; Bassett, W. A.; Chou, I. M. Steric Hindrance and the Enhanced Stability of Light Rare-Earth Elements in Hydrothermal Fluids. *Am. Mineral.* **2009**, *94*, 1487−1490.
(166) Mayanovic, R. A.; Anderson, A. J.; Bassett, W. A.; Chou, I. M. The Structure and Stability of Aqueous Rare-Earth Elements in Hydrothermal Fluids: New Results on Neodymium(III) Aqua and Chloroaqua Complexes in Aqueous Solutions to 500 °C and 520 MPa. *Chem. Geol.* **2009**, *259*, 30−38.
(167) Strzelecki, A. C.; Migdisov, A.; Boukhalfa, H.; Sauer, K.; McIntosh, K. G.; Currier, R. P.; Williams-Jones, A. E.; Guo, X. Fluocerite as a Precursor to Rare Earth Element Fractionation in Ore-Forming Systems. *Nat. Geosci.* **2022**, *15*, 327−333.
(168) Leitner, J.; Sedmidubsky, D.; Ruzicka, K.; Svobo, P. Calorimetric Determination of Heat Capacity, Entropy and Enthalpy of Mixed Oxides in the System $CaO−SrO−Bi_2O_3−Nb_2O_5−Ta_2O_5$. In *Applications of Calorimetry in a Wide Context - Differential Scanning Calorimetry, Isothermal Titration Calorimetry and Microcalorimetry*; Elkordy, A. A., Ed.; BoD − Books on Demand, 2013; pp. 385−406.
(169) Konings, R. J. M.; Beneš, O.; Kovács, A.; Manara, D.; Sedmidubskỳ, D.; Gorokhov, L.; Iorish, V. S.; Yungman, V.; Shenyavskaya, E.; Osina, E. The Thermodynamic Properties of the F-Elements and Their Compounds. Part 2. The Lanthanide and Actinide Oxides. *J. Phys. Chem. Ref. Data* **2014**, *43*, No. 013101.
(170) Zhao, Z.; Chen, H.; Xiang, H.; Dai, F. Z.; Wang, X.; Peng, Z.; Zhou, Y. $(La_{0.2}Ce_{0.2}Nd_{0.2}Sm_{0.2}Eu_{0.2})PO_4$: A High-Entropy Rare-Earth Phosphate Monazite Ceramic with Low Thermal Conductivity and Good Compatibility with Al_2O_3. *J. Mater. Sci. Technol.* **2019**, *35*, 2892−2896.
(171) Navrotsky, A. *Physics and Chemistry of Earth Materials*; Cambridge University Press, 1994.
(172) McCormack, S. J.; Navrotsky, A. Thermodynamics of High Entropy Oxides. *Acta Mater.* **2021**, *202*, 1−21.
(173) George, E. P.; Raabe, D.; Ritchie, R. O. High-Entropy Alloys. *Nat. Rev. Mater.* **2019**, *4*, 515−534.

https://doi.org/10.1021/acsearthspacechem.2c00052
ACS Earth Space Chem. 2022, 6, 1375−1389